

NASA TECHNICAL NOTE

NASA TN D-5048



NASA TN D-5048

C. 1

949946



TECH LIBRARY KAFB, NM

LOAN COPY: RETURN TO  
AFWL (WLIL-2)  
KIRTLAND AFB, N MEX

EFFECTS OF CONE ANGLE, BASE  
FLARE ANGLE, AND CORNER RADIUS ON  
MACH 3.0 AERODYNAMIC CHARACTERISTICS  
OF LARGE-ANGLE CONES

by William D. Deveikis and James Wayne Sawyer  
Langley Research Center  
Langley Station, Hampton, Va.

TECH LIBRARY KAFB, NM



0131946

EFFECTS OF CONE ANGLE, BASE FLARE ANGLE, AND  
CORNER RADIUS ON MACH 3.0 AERODYNAMIC CHARACTERISTICS  
OF LARGE-ANGLE CONES

By William D. Deveikis and James Wayne Sawyer

Langley Research Center  
Langley Station, Hampton, Va.

NATIONAL AERONAUTICS AND SPACE ADMINISTRATION

---

For sale by the Clearinghouse for Federal Scientific and Technical Information  
Springfield, Virginia 22151 - CFSTI price \$3.00

EFFECTS OF CONE ANGLE, BASE FLARE ANGLE, AND  
CORNER RADIUS ON MACH 3.0 AERODYNAMIC CHARACTERISTICS  
OF LARGE-ANGLE CONES

By William D. Deveikis and James Wayne Sawyer  
Langley Research Center

SUMMARY

A wind-tunnel investigation was conducted on large-angle cones to determine the effects on static aerodynamic characteristics of cone angles from  $110^\circ$  to  $150^\circ$ , base flare angles from  $65^\circ$  to  $90^\circ$ , and base corner radii to 20 percent of the base radius. The tests were conducted at angles of attack to  $12^\circ$  and at Reynolds numbers, based on maximum body diameter, of approximately  $1.1 \times 10^6$  and  $3.0 \times 10^6$  in a Mach 3.0 stream. All models were statically stable, and aerodynamic centers were located downstream from the base. The static stability was relatively insensitive to cone angle but decreased as the flare angle and corner radius increased. The axial-force coefficient increased with cone angle and flare angle but decreased with increasing corner radius.

INTRODUCTION

A number of investigations on high-drag bodies have shown that the large-angle cone has a relatively high drag capability and is statically stable over a wide range of Mach numbers (refs. 1 to 3). Consequently, the large-angle cone has emerged as a configuration of interest for atmospheric-entry vehicle systems (ref. 4). The present investigation considers some of the geometric variables that can affect the static longitudinal aerodynamic characteristics of large-angle cones and was undertaken to determine the influence of large variations in cone angle, base flare angle, and base corner radius.

Families of shapes with cone angles between  $110^\circ$  and  $150^\circ$ , base flare angles between  $65^\circ$  and  $90^\circ$ , and base corner radii up to 20 percent of the base radius were tested at angles of attack up to  $12^\circ$  to obtain schlieren data and static force and pitching-moment measurements. The tests were conducted in the Langley 9- by 6-inch model tunnel at a Mach number of 3.0, and at Reynolds numbers based on maximum body diameter of  $1.1 \times 10^6$  and  $3.0 \times 10^6$ .

## SYMBOLS

The units used for the physical quantities in this paper are given both in the U.S. Customary Units and in the International System of Units (SI). Factors relating the two systems are given in reference 5, and those used in the present investigation are presented in appendix A.

A area

$A_b$  projected model base area,  $\pi r_b^2$

$C_A$  axial-force coefficient,  $\frac{\text{Axial force}}{q_\infty A_b}$

$C_N$  normal-force coefficient,  $\frac{\text{Normal force}}{q_\infty A_b}$

$C_{N\alpha}$  slope of the normal-force curve at zero angle of attack, per degree,  

$$\left(\frac{\partial C_N}{\partial \alpha}\right)_{\alpha=0^\circ}$$

$C_m$  pitching-moment coefficient,  $\frac{\text{Pitching moment}}{2q_\infty A_b r_b}$

$C_{m\alpha}$  slope of the pitching-moment curve at zero angle of attack, per degree,  

$$\left(\frac{\partial C_m}{\partial \alpha}\right)_{\alpha=0^\circ}$$

$C_p$  pressure coefficient,  $\frac{p_l - p_\infty}{q_\infty}$

D drag force

K Newtonian constant

M Mach number

$p_l$  local surface pressure

$p_\infty$  free-stream static pressure

$q_\infty$  free-stream dynamic pressure

R Reynolds number based on maximum body diameter

$r$	radial coordinate (fig. 1)
$r_b$	model base radius
$r_c$	corner radius at model base
$r_f$	forebody maximum radius
$r_n$	spherical nose radius
$x$	axial coordinate (fig. 1)
$x_{ac}$	axial coordinate of aerodynamic center, $\left(\frac{C_{m\alpha}}{C_{N\alpha}}\right)2r_b$
$\alpha$	angle of attack
$\beta$	local surface angle with respect to body axis
$\delta$	flare angle
$\theta$	cone apex angle
$\sigma$	detached shock-wave standoff distance, measured along geometric center line from cone apex

### MODELS, APPARATUS, AND TESTS

#### Models

The three groups of models for this investigation are illustrated in figure 1. One group consisted of four cones with apex angles of  $110^\circ$ ,  $130^\circ$ ,  $140^\circ$ , and  $150^\circ$ . Each model in this group was spherically blunted to  $r_n/r_b = 0.20$ . In the second group, a flared skirt was added to the base of six  $120^\circ$  cones at angles from  $65^\circ$  to  $90^\circ$  in  $5^\circ$  increments. The cone-flare juncture was located at a position at which the ratio of local radius to base radius,  $r_f/r_b$ , was 0.707, so that the total projected area was double that of the  $120^\circ$ -cone forebody. For the flared-cone models, the nose radius was zero. In the third group, the corner was rounded at the base of four  $120^\circ$ -cone models, so that  $r_c/r_b = 0.05, 0.10, 0.15$ , and  $0.20$ . These models were spherically blunted to  $r_n/r_b = 0.20$ .

The base radius for all models was 0.625 inch (1.59 cm). The models were machined from 17-4 PH stainless steel and were polished to a finish of approximately 10 microinches (254 nm), rms.

### Test Facility

The tests were conducted in the Langley 9- by 6-inch model tunnel (ref. 6). This facility is a supersonic (Mach 3.0) blowdown wind tunnel with an air storage and pumping capacity sufficient to permit continuous operation at ambient stagnation temperature. The tunnel stagnation-pressure operating range is from 55 to 200 pounds per square inch absolute (380 to 1380 kN/m<sup>2</sup>), and the stagnation temperature range is from ambient to 3000° F (1900° K). Calibration tests of the tunnel test section showed a maximum deviation in Mach number of less than 1 percent.

### Instrumentation

Aerodynamic forces and pitching moments were measured with an externally mounted, three-component, strain-gage sting-balance assembly that was shielded from the airstream by means of a shroud. The shroud diameter was held constant at 0.55 inch (1.40 cm) for four model base diameters and then flared outward at an included angle of 29°. The exposed sting length between the model base and the shroud varied from approximately  $0.10r_b$  for the cone models with round corners to approximately  $0.34r_b$  for the other models because of the mounting shank at the model base (fig. 1). For this range of exposed sting lengths, no measurable variations in balance output were encountered.

Model base pressure was measured in the yaw plane at a location approximately  $0.10r_b$  downstream from the model base by means of an orifice tube attached along the outer surface of the sting-balance shroud. With the orifice-tube diameter included, the ratio of the shroud diameter to the model base diameter was approximately 0.49. Output from pressure transducers and strain-gage balance was recorded by the Langley central digital data recording facility.

Angle of attack was indicated by a digital voltmeter which recorded the output from a linear potentiometer attached to an angle-of-attack mechanism capable of pitching the models from -1° through 12°. The angle-of-attack readings do not take flow angularity into account or sting deflection due to model air loads, but static load calculations show that the sting deflection should not exceed 0.3°. Shock waves and flow patterns generated by the model shapes were recorded photographically with the aid of a single-pass horizontal Z-light path schlieren system and a spark light-source duration of approximately 0.2 microsecond.

### Test Procedure

Stagnation dewpoint was maintained at  $-98^{\circ}$  F ( $201^{\circ}$  K) to avoid condensation effects in the test section. All tests were conducted at ambient stagnation temperatures and at stagnation pressures of 65 and 170 pounds per square inch absolute ( $448$  and  $1172$  kN/m $^2$ ). Corresponding Reynolds numbers, based on maximum body diameter, were approximately  $1.1 \times 10^6$  and  $3.0 \times 10^6$ . All models were tested at angles of attack between  $-1^{\circ}$  and  $12^{\circ}$ , and in each test, the tunnel was operated continuously throughout the angle-of-attack range at both stagnation-pressure levels.

The test procedure was to start the tunnel with the model at zero angle of attack. When supersonic flow conditions were established in the test section, data were recorded at the low and then at the high stagnation-pressure level at each angle of attack. Data were recorded for 5 seconds at each stagnation-pressure level to insure an equilibrium base-pressure response. Prior to termination of a test, data were recorded a second time at angles of attack of  $-1^{\circ}$  and  $1^{\circ}$  to determine whether shifts in the balance output had occurred. No data were acquired during the change from one angle of attack to another.

### Data

Prior to the present tests, the strain-gage balance was regaged and recalibrated to compensate for a nonuniform temperature distribution along the length of the sting-balance assembly and for the low-temperature environment in the test section. This work was done as part of an effort to isolate the causes of a zero shift that occurred in the balance output between no-flow and flow conditions in previous investigations. (See, for example, ref. 1.) Nevertheless, in the present tests, a shift in the balance output was again encountered during the time interval between no-flow and flow conditions such that nonzero values of the pitching-moment and normal-force coefficients were obtained at  $\alpha = 0^{\circ}$ . However, inasmuch as the data for the low values of  $\alpha$  obtained at the beginning and just prior to the end of a test showed excellent repeatability for all models, the slopes of the curves of  $C_m$  and  $C_N$  as functions of  $\alpha$  used in determining  $C_{m\alpha}$  and  $C_{N\alpha}$  are considered valid.

All experimental axial-force data presented herein have been corrected to a free-stream static-pressure condition at the model base. The actual measured values of  $C_A$  were from 0.10 to 0.13 higher than shown, as determined from base-pressure measurements. Thus, the measured base-drag coefficients bracket the parameter  $1/M^2$  often used as a base-pressure correction factor; the base-drag coefficients gradually decreased with angle of attack within approximately 10 percent at  $\alpha = 12^{\circ}$ . The moment center was located at the base of the cones, at the cone-flare juncture for the flared cones, and at the

base of a cone with zero corner radius for the round-cornered cones. (See fig. 1.) Estimated accuracies of the measured data based on 0.5 percent of full load for each balance component are as follows:

	$R \approx 1.1 \times 10^6$	$R \approx 3.0 \times 10^6$
$C_A$ . . . . .	$\pm 0.024$	$\pm 0.008$
$C_m$ . . . . .	$\pm 0.010$	$\pm 0.004$
$C_N$ . . . . .	$\pm 0.008$	$\pm 0.002$

## RESULTS AND DISCUSSION

### Flow Patterns

Typical schlieren photographs of the large-angle cones, the flared cones, and the round-cornered cones are shown in figures 2 to 7 for  $\alpha = 0^\circ$  and  $120^\circ$  at both Reynolds numbers. Photographs of a  $120^\circ$  cone with zero nose radius from reference 1 are included. All models generated a detached bow shock wave, but some differences are noted in its shape and standoff distance. As the cone angle and flare angle increase, the shock-wave shape flattens, and the shock standoff distance increases, whereas the effect of corner radius appears insignificant.

The effects of cone angle, base flare angle, and base corner radius on the shock-wave standoff distance are summarized in figure 8. Included are test data from the  $120^\circ$ -cone models of references 1 and 7 with  $r_n/r_b = 0$ ; these data show good agreement with the present data for  $r_n/r_b = 0$ . The dashed lines are computed values obtained from the integral-relations method of reference 8. This method can compute the shock-wave standoff distance, the shock-wave shape to the sonic point, the local flow conditions along the surface, and the axial force on blunt bodies. The method was not applied to the round-cornered cones because the computer program of reference 8 provided solutions only for shapes with sonic corners. In order to apply the method to the cone-flare problem, a small nose radius ( $0.05r_b$ ) and a fillet radius ( $0.55r_b$ ) at the cone-flare juncture were assumed because the method cannot negotiate a discontinuity in the flow direction.

The results indicate that the shock-wave standoff distance increases linearly as the cone angle and flare angle increase, decreases slightly as the corner radius and Reynolds number increase, and increases with nose radius (see  $\theta/2 = 60^\circ$ ). The largest shock-wave standoff distances are shown by the cones; the smallest, by the round-cornered cones. The computed values show good agreement with the measured values at all cone angles and at the smaller flare angles; the difference between the measured and computed values grows, however, with increasing flare angle such that at  $\delta = 90^\circ$ , the computed shock-wave standoff distance is approximately 20 percent less than the measured value.

The computed shock-wave standoff distances affect the agreement between the computed and measured shock-wave shapes as shown in figure 9 for the cones and in figure 10 for the flared cones. In general, the shock-wave shapes are approximated very well by the integral-relations method, but the differences between the measured and computed values appear to grow with increasing cone and flare angles, primarily because of the increasing differences in the measured and computed shock-wave standoff distances. In the cone-flare problem, an additional source of disagreement is provided by the flare in that the slopes of the computed shock waves decrease at the point influenced by the cone-flare juncture (tick marks, fig. 10). This effect becomes more pronounced with increasing flare angle.

#### Effect of Cone Angle on Aerodynamic Characteristics

Variations of the pitching-moment, axial-force, and normal-force coefficients with angle of attack at  $R \approx 1.1 \times 10^6$  and  $3.0 \times 10^6$  are shown in figure 11 for cone angles between  $110^\circ$  and  $150^\circ$ . Included are data from reference 1 for a  $120^\circ$  cone with zero nose radius. The results indicate an increase in the axial-force coefficient with increasing cone angle. For each cone angle, the axial-force coefficient decreases slightly with angle of attack; but as the cone angle increases, the change in  $C_A$  with  $\alpha$  becomes progressively smaller. Although the slopes of the  $C_m$  curves are not appreciably affected by increasing the cone angle, the slopes of the  $C_N$  curves decrease substantially. An increase in the Reynolds number to approximately  $3.0 \times 10^6$  resulted in a small reduction in  $C_A$  (approximately 2 percent).

In figure 12, the increase in  $C_A$  at  $\alpha = 0^\circ$  between  $\theta = 110^\circ$  and  $150^\circ$  amounts to approximately 11.5 percent, and a straight line faired through the data indicates a  $C_A$  rise per degree cone half-angle of 0.009. The values of the parameter  $C_{m\alpha}$  appear relatively insensitive to cone angle but indicate static stability for cone angles in the present range. Outside of this range of cone angles, Newtonian theory predicts an increase in  $C_{m\alpha}$  to positive values. (See ref. 7.) This trend has been experimentally verified somewhat in reference 7 and is also suggested by the present values at  $\theta = 110^\circ$  and  $150^\circ$ . The values of the parameter  $C_{N\alpha}$  decrease with increasing cone angle with the result that the aerodynamic center  $x_{ac}$  moves downstream. As shown in figure 12, the aerodynamic centers are located downstream from the base.

In figure 12, the data are consistent with respect to Reynolds number except for the  $C_{m\alpha}$  and  $C_{N\alpha}$  data from the reference  $120^\circ$  cone. A similar inconsistency appears subsequently in the  $C_{m\alpha}$  data from the flared cone with a  $65^\circ$  flare angle. These discrepancies are attributed to the very small quantities measured and to limitations on the measurement accuracy.

As shown in figure 12, the calculated values of  $C_A$  at  $\alpha = 0^\circ$  obtained from Newtonian theory lie on a curve for which the slope is considerably greater than that shown by the test points with the result that the test values are increasingly overpredicted for  $\theta > 120^\circ$ . At  $\theta = 150^\circ$ , the Newtonian value of  $C_A$  is approximately 21 percent greater than the test value. Somewhat better agreement is obtained with the modified Newtonian theory (within  $8\frac{1}{2}$  percent for  $\theta$  between  $120^\circ$  and  $150^\circ$ ), but the slope obtained of the  $C_A$  variation with  $\theta$  remains considerably greater than that of the test points. The equations used in obtaining the Newtonian values are derived in appendix B. A value of 2 was used for the constant  $K$  in the Newtonian theory and 1.755 in the modified Newtonian theory. The latter value is the pressure coefficient evaluated behind a normal shock for  $M = 3$ . The trend of the experimental data is much better predicted with the aid of the integral-relations method of reference 8, and calculated values that average within  $3\frac{1}{2}$  percent less than the test values are obtained. The better agreement provided by this method is attributed to the accuracy with which the shock shape (fig. 9), standoff distance (fig. 8), and local flow conditions at the surface can be determined.

#### Effect of Base Flare Angle on Aerodynamic Characteristics

The addition of a flared skirt at the base of a  $120^\circ$  cone causes an increase in the axial-force coefficient, as is shown in figure 13. Although an increase in the flare angle does not affect the slope of the variation of  $C_A$  with  $\alpha$ , the negative  $C_m$  slopes and the positive  $C_N$  slopes decrease; hence, a trend unfavorable to static stability is indicated. For  $\delta$  between  $65^\circ$  and  $90^\circ$ , the value of  $C_A$  at  $\alpha = 0^\circ$  increases by approximately 9 percent to a value approximating that obtained with the flat circular disk model of reference 9. (See fig. 14.) With respect to the reference  $120^\circ$  cone, the increase in  $C_A$  varies from approximately 6 to 15 percent over the present range of flare angles. A straight line faired through the  $C_A$  data indicates a rise in  $C_A$  per degree flare angle of 0.006, or about two-thirds the rate obtained by increasing the angle of unflared cones. However, the increase in  $C_A$  due to the flared skirt is offset somewhat by a corresponding decrease in static stability, as shown by the decreasing negative  $C_{m\alpha}$  values. At  $\delta = 90^\circ$ ,  $C_{m\alpha}$  is about one-half the value for the reference  $120^\circ$  cone. The  $C_{N\alpha}$  values also decrease with the result that the location of the aerodynamic center shifts downstream as the flare angle increases. As shown in figure 14, the aerodynamic centers are located downstream from the base. An increase in the Reynolds number to approximately  $3.0 \times 10^6$  resulted in a decrease in  $C_A$  within 4 percent.

Calculated values of  $C_A$  at  $\alpha = 0^\circ$  obtained from the Newtonian, modified Newtonian, and integral-relations methods predict the data trend reasonably well, as shown in figure 14. In this case, the values of  $C_A$  calculated from the Newtonian theory averaged approximately  $6\frac{1}{2}$  percent greater than the test values, whereas the values

calculated from the modified Newtonian theory and the integral-relations method averaged 7 and 5 percent, respectively, less than the test values. The agreement between the values from the integral-relations method and the test data is not as good as obtained with the cones because of the effects on the computed flow conditions at the surface resulting from the discrepancies encountered between the computed and measured shock-wave shapes and standoff distances (see figs. 8 and 9) in the cone-flare problem.

A comparison of the data from the flared cones and cones of equal flow turning angle is shown in figure 15. For this comparison, the moment center of the flared cones was moved to the base to provide correspondence with the moment center location of the cones. With respect to the cones, the flared cones indicate slightly higher  $C_A$  values, approximately the same static stability, somewhat greater  $C_{N\alpha}$  values, and aerodynamic centers that are located farther upstream. Calculated values of  $C_A$  from the integral-relations method of reference 8 indicate higher values for the cones.

#### Effect of Base Corner Radius on Aerodynamic Characteristics

Rounding the corner at the base of a  $120^\circ$  cone results in decreasing the axial-force coefficient as shown in figure 16. Increasing the corner radius has little effect on the slopes of the  $C_m$  and  $C_A$  curves but results in increasing the slopes of the  $C_N$  curves. The  $C_A$  values at  $\alpha = 0^\circ$  decrease linearly with increasing corner radius as shown in figure 17, and with respect to the reference  $120^\circ$  cone ( $r_n/r_b = 0$  and  $r_c/r_b = 0$ ), the loss in drag at  $r_c/r_b = 0.20$  amounts to about 8 percent. An increase in the Reynolds number to approximately  $3.0 \times 10^6$  resulted in reducing  $C_A$  by approximately 4 percent. The negative values of the parameter  $C_{m\alpha}$  indicate static stability for all corner radii and appear relatively unaffected by corner radius. Although the parameter  $C_{N\alpha}$  increases with corner radius, the location of the aerodynamic center (downstream of the base) appears insensitive to corner radius.

Calculated values from Newtonian and modified Newtonian theories predict the trend of the data but are approximately 8 percent greater and 6 percent less than the test values, respectively. The integral-relations method was not applied to the round-cornered cones because the computer program of reference 8 provided solutions only for those shapes for which the sonic point occurs at a sharp corner.

#### CONCLUSIONS

A wind-tunnel investigation was conducted on large-angle cones at a Mach number of 3.0 and at Reynolds numbers, based on maximum body diameter, of approximately  $1.1 \times 10^6$  and  $3.0 \times 10^6$  to determine the effects on static aerodynamic characteristics of cone angle, base flare angle, and base corner radius. The test results indicated the following conclusions:

1. All models were statically stable. The static stability was relatively insensitive to cone angle and corner radius but decreased as the flare angle increased.
2. Increasing the cone angle from  $110^\circ$  to  $150^\circ$  caused the axial-force coefficient at zero angle of attack to increase approximately 11.5 percent.
3. Increasing the flare angle at the base of a  $120^\circ$  cone from  $65^\circ$  to  $90^\circ$  caused the axial-force coefficient at zero angle of attack to increase approximately 9 percent, and at a flare angle of  $90^\circ$ , the axial-force coefficient at zero angle of attack approximated that of the flat circular disk.
4. Increasing the corner radius at the base of a  $120^\circ$  cone to 20 percent of the base radius caused the axial-force coefficient at zero angle of attack to decrease approximately 8 percent.
5. Axial-force coefficients obtained from Newtonian theory were up to 21 percent higher than experiment for the cones, were approximately  $6\frac{1}{2}$  percent higher for the flared cones, and were approximately 8 percent greater for the cones with round corners at the base.
6. Axial-force coefficients obtained from the modified Newtonian theory were within  $8\frac{1}{2}$  percent of experimental values for cone angles between  $120^\circ$  and  $150^\circ$ , were approximately 7 percent less than experiment for the flared cones, and were approximately 6 percent less than experiment for the cones with round corners at the base.
7. Axial-force coefficients obtained from an integral-relations method were within  $3\frac{1}{2}$  percent less than experiment for the cones and were approximately 5 percent less than experiment for the flared cones.
8. The aerodynamic center was located downstream from the base of all models; it shifted downstream with increasing cone angle and flare angle but appeared relatively insensitive to corner radius.
9. As the cone angle and flare angle increased, the detached shock-wave standoff distance increased linearly, but the standoff distance was considerably greater for the cones. The standoff distance tended to decrease slightly as the corner radius increased.
10. An increase in the Reynolds number from  $1.1 \times 10^6$  to  $3.0 \times 10^6$  was accompanied by a decrease in the axial-force coefficient within 2 percent for the cones and within 4 percent for the flared cones and those with rounded corners.

Langley Research Center,  
National Aeronautics and Space Administration,  
Langley Station, Hampton, Va., December 18, 1968,  
124-08-06-03-23.

## APPENDIX A

### CONVERSION OF U.S. CUSTOMARY UNITS TO SI UNITS

Conversion factors required for units used herein are taken from reference 5 and presented in the following table:

Physical quantity	U.S. Customary unit	Conversion factor (a)	SI unit
Length . . . . .	in.	0.0254	meters (m)
Pressure . . . . .	psi	$6.895 \times 10^3$	newtons/meter <sup>2</sup> (N/m <sup>2</sup> )
Temperature . . .	(F° + 460)	5/9	degrees Kelvin (°K)

<sup>a</sup>Multiply value given in U.S. Customary unit by conversion factor to obtain equivalent value in SI units.

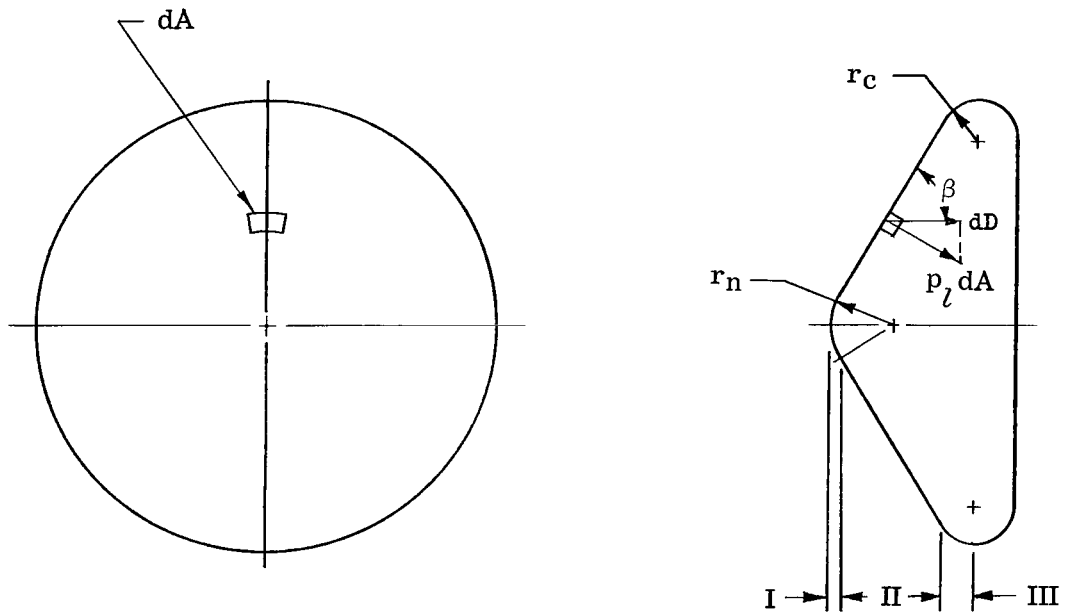
Prefixes to indicate multiples of units are as follows:

Prefixes	Multiple
centi (c)	$10^{-2}$
kilo (k)	$10^3$
nano (n)	$10^{-9}$

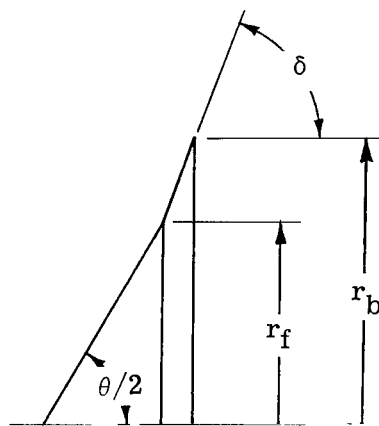
## APPENDIX B

### NEWTONIAN EQUATIONS

The geometrical parameters associated with the families of axisymmetric bodies of the present investigation are defined in the following sketches:



Sketch 1



Sketch 2

## APPENDIX B

The differential drag resulting from a pressure  $p_l$  acting on a differential surface area  $dA$  can be expressed as

$$dD = p_l \sin \beta dA \quad (1)$$

where  $\beta$  is the local surface angle with respect to the cone axis. The total drag then becomes

$$D = \int_A p_l \sin \beta dA = \int_{\text{nose}} p_l \sin \beta dA + \int_{\text{base}} p_l \sin \beta dA \quad (2)$$

In order to present equation (2) in the form of pressure coefficients, the expression

$$\int_A p_\infty \sin \beta dA = 0$$

is used in conjunction with equation (2) to obtain

$$D = \int_{\text{nose}} (p_l - p_\infty) \sin \beta dA + \int_{\text{base}} (p_l - p_\infty) \sin \beta dA \quad (3)$$

The nose region is defined as extending from the tip to the maximum radius. If the base pressure is assumed equal to  $p_\infty$ , equation (3) becomes

$$D = \int_{\text{nose}} (p_l - p_\infty) \sin \beta dA \quad (4)$$

In terms of the axial-force coefficient and the pressure coefficient, equation (4) becomes

$$C_A = \frac{1}{A_b} \int_{\text{nose}} C_p \sin \beta dA \quad (5)$$

From Newtonian theory, the pressure coefficient can be expressed as

$$C_p = K \sin^2 \beta \quad (6)$$

which, when substituted into equation (5), gives

$$C_A = \frac{K}{A_b} \int_{\text{nose}} \sin^3 \beta dA \quad (7)$$

The differential area  $dA$  for the nose region can be expressed in terms of  $\beta$  and  $r$  to obtain integral expressions for each configuration. Thus, for the spherical cap of the cones with zero and nonzero corner radii at the base (region I of sketch 1),

$$\frac{\theta}{2} \leq \beta \leq \frac{\pi}{2}$$

## APPENDIX B

$$r_n \cos \frac{\theta}{2} \geq r \geq 0$$

and

$$dA = 2\pi r_n^2 \cos \beta \, d\beta \quad (8a)$$

For the conical portion (region II of sketch 1),

$$\beta = \frac{\theta}{2}$$

$$r_n \cos \frac{\theta}{2} \leq r \leq r_b \quad (\text{when } r_c = 0)$$

$$r_n \cos \frac{\theta}{2} \leq r \leq r_b - r_c + r_c \cos \frac{\theta}{2} \quad (\text{when } r_c \neq 0)$$

and

$$dA = \frac{2\pi}{\sin \frac{\theta}{2}} r \, dr \quad (8b)$$

For the round corner (region III of sketch 1),

$$0 \leq \beta \leq \frac{\theta}{2}$$

$$r_b \geq r \geq r_b - r_c + r_c \cos \frac{\theta}{2}$$

and

$$dA = 2\pi r_c (r_b - r_c + r_c \cos \beta) d\beta \quad (8c)$$

For the sharp-nose cone forebody of the cones with flared skirts (sketch 2),

$$\beta = \frac{\theta}{2}$$

$$0 \leq r \leq r_f$$

and

$$dA = \frac{2\pi}{\sin \frac{\theta}{2}} r \, dr \quad (9a)$$

For the flared skirt (sketch 2),

$$\beta = \delta$$

$$r_f \leq r \leq r_b$$

## APPENDIX B

and

$$dA = \frac{2\pi}{\sin \delta} r dr \quad (9b)$$

Combining equation (7) with equations (8) and (9) results in the following integral expressions for the axial-force coefficient:

For the spherically capped cone with zero corner radius,

$$C_A = \frac{K}{A_b} \left[ 2\pi r_n^2 \int_{\theta/2}^{\pi/2} \sin^3 \beta \cos \beta d\beta + 2\pi \sin^2(\theta/2) \int_{r_n \cos(\theta/2)}^{r_b} r dr \right] \quad (10)$$

For the spherically capped cone with round corners at the base,

$$C_A = \frac{K}{A_b} \left[ 2\pi r_n^2 \int_{\theta/2}^{\pi/2} \sin^3 \beta \cos \beta d\beta + 2\pi \sin^2(\theta/2) \int_{r_n \cos(\theta/2)}^{r_b - r_c + r_c \cos(\theta/2)} r dr \right. \\ \left. + 2\pi r_c \int_0^{\theta/2} (r_b - r_c + r_c \cos \beta) \sin^3 \beta d\beta \right] \quad (11)$$

For the sharp-nose cone with flared skirt,

$$C_A = \frac{K}{A_b} \left[ 2\pi \sin^2(\theta/2) \int_0^{r_f} r dr + 2\pi \sin^2 \delta \int_{r_f}^{r_b} r dr \right] \quad (12)$$

Integrating equations (10), (11), and (12) and rearranging terms yields the following:

For the spherically capped cone with zero corner radius,

$$C_A = \frac{K}{2} \left( \frac{r_n}{r_b} \right)^2 \left[ 1 - \sin^4(\theta/2) \right] + K \sin^2(\theta/2) \left[ 1 - \left( \frac{r_n}{r_b} \right)^2 \cos^2(\theta/2) \right] \quad (13)$$

For the spherically capped cone with round corners at the base,

$$C_A = \frac{K}{2} \left( \frac{r_n}{r_b} \right)^2 \left[ 1 - \sin^4(\theta/2) \right] + K \sin^2(\theta/2) \left\{ \left[ 1 - \frac{r_c}{r_b} + \frac{r_c}{r_b} \cos(\theta/2) \right]^2 - \left( \frac{r_n}{r_b} \right)^2 \cos^2(\theta/2) \right\} \\ + 2K \left( \frac{r_c}{r_b} \right) \left( 1 - \frac{r_c}{r_b} \right) \left\{ \frac{2}{3} - \frac{1}{3} \cos(\theta/2) \left[ \sin^2(\theta/2) + 2 \right] \right\} + \frac{K}{2} \left( \frac{r_c}{r_b} \right)^2 \sin^4(\theta/2) \quad (14)$$

## APPENDIX B

For the sharp-nose cone with flared skirt,

$$C_A = K \sin^2 \delta + K \left( \frac{r_f}{r_b} \right)^2 \left[ \sin^2(\theta/2) - \sin^2 \delta \right] \quad (15)$$

## REFERENCES

1. Sawyer, James Wayne: Comparison of the Mach 3.0 Aerodynamic Characteristics of Tension String, Tension Shell, and 120° Conical Shapes. NASA TN D-4360, 1968.
2. Harris, Charles D.: Transonic Aerodynamic Investigation of Tension Shell and Blunted 100° Conical Shapes for Unmanned Entry Vehicles. NASA TN D-3700, 1966.
3. Campbell, James F.: Longitudinal Aerodynamic Characteristics of Several High-Drag Bodies at Mach Numbers From 1.50 to 4.63. NASA TN D-3915, 1967.
4. Guy, L. D.: Structural Design Options for Planetary Entry. AIAA Paper No. 68-344, Apr. 1968.
5. Comm. on Metric Pract.: ASTM Metric Practice Guide. NBS Handbook 102, U.S. Dep. Com., Mar. 10, 1967.
6. Schaefer, William T., Jr.: Characteristics of Major Active Wind Tunnels at the Langley Research Center. NASA TM X-1130, 1965.
7. Campbell, James F.; and Howell, Dorothy T.: Supersonic Aerodynamics of Large-Angle Cones. NASA TN D-4719, 1968.
8. South, Jerry C., Jr.: Calculation of Axisymmetric Supersonic Flow Past Blunt Bodies With Sonic Corners, Including a Program Description and Listing. NASA TN D-4563, 1968.
9. Sawyer, James Wayne; and Deveikis, William D.: Effects of Configuration Modifications on Aerodynamic Characteristics of Tension Shell Shapes at Mach 3.0. NASA TN D-4080, 1967.



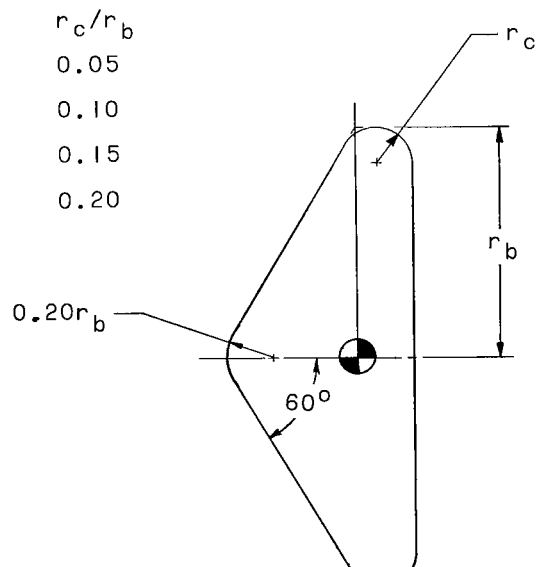
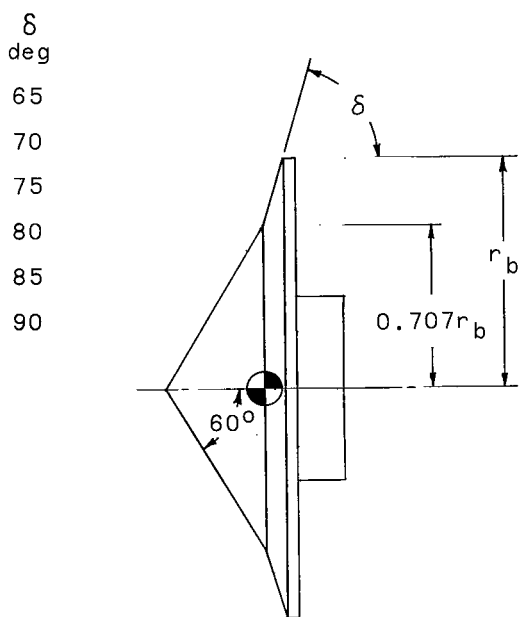
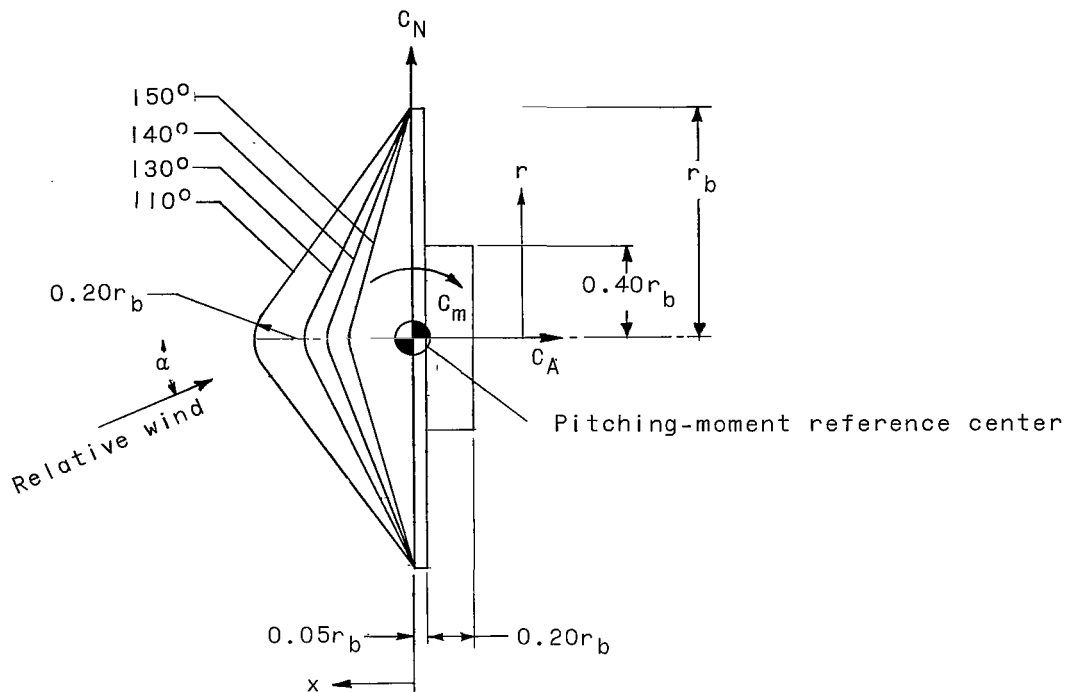
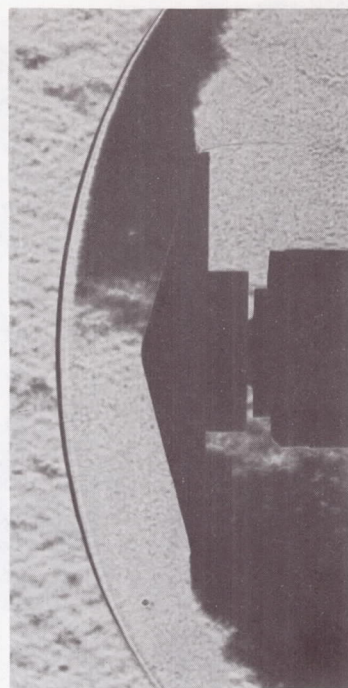
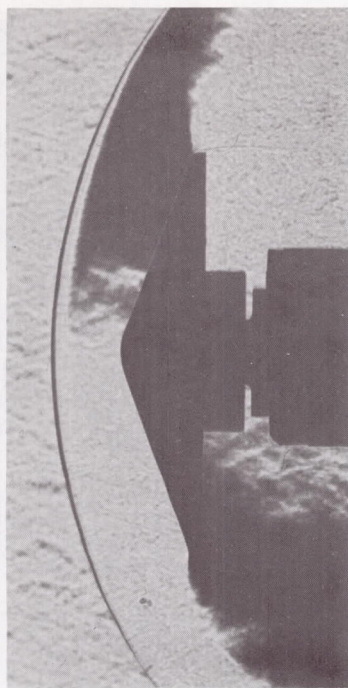
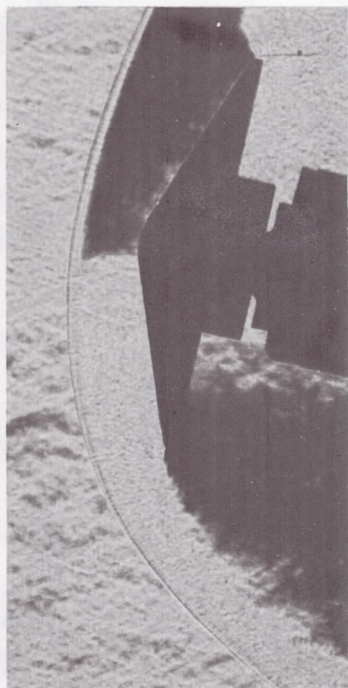


Figure 1.- Model details and body-axis system. Arrows indicate positive directions. Base radius, 0.625 in. (1.59 cm).

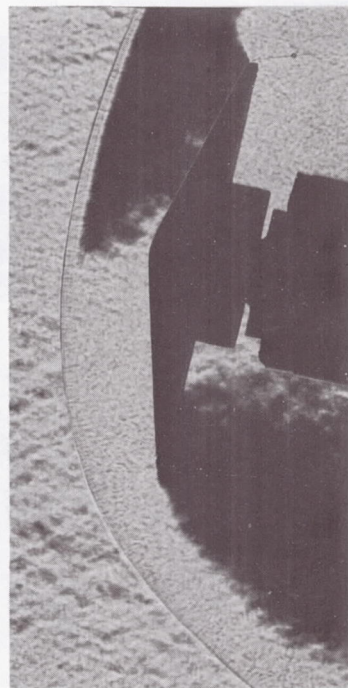
$\alpha = 0^\circ$



$\alpha = 12^\circ$



$140^\circ$  Cone

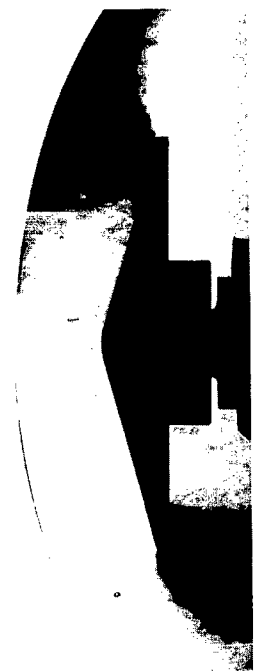
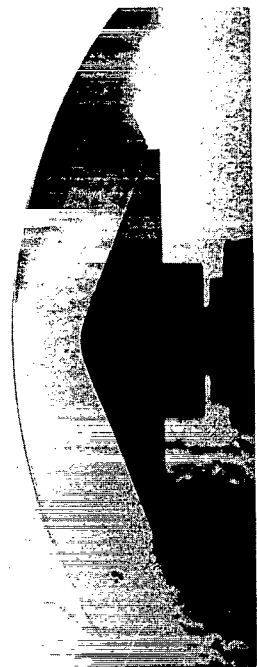


$150^\circ$  Cone

Figure 3.- Concluded.

L-68-10,084

$\alpha = 0^\circ$



$\alpha = 12^\circ$



$140^\circ$  Cone



$150^\circ$  Cone

Figure 2.- Concluded.

L-68-10,082

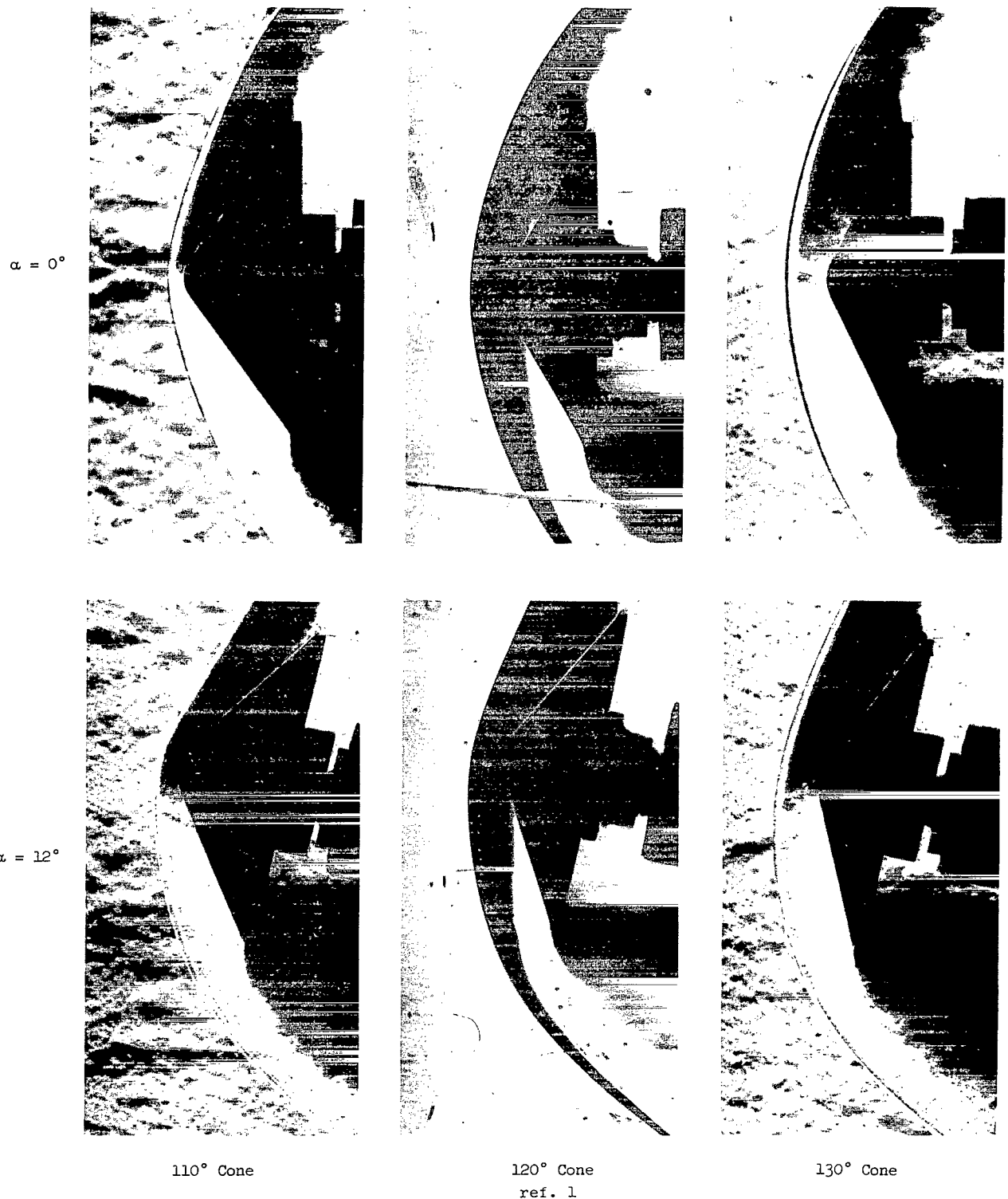
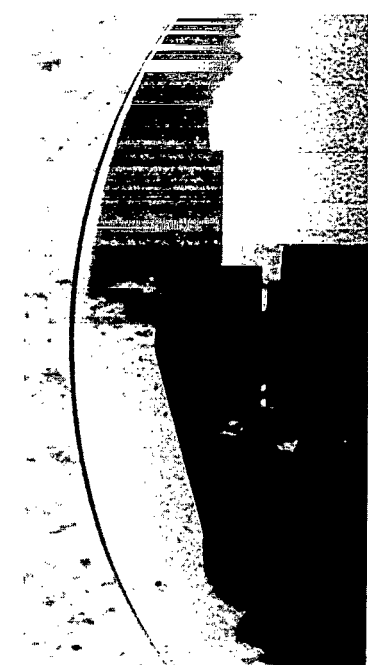


Figure 3.- Schlieren photographs of large-angle cones at  $R \approx 3.0 \times 10^6$  and Mach 3.0.

L-68-10,083

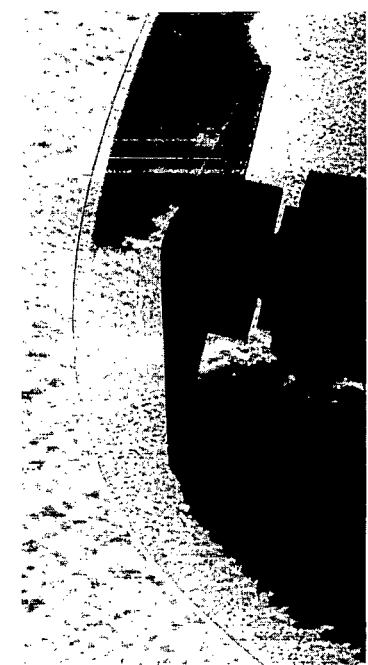
$\alpha = 0^\circ$



$\alpha = 12^\circ$



$140^\circ$  Cone

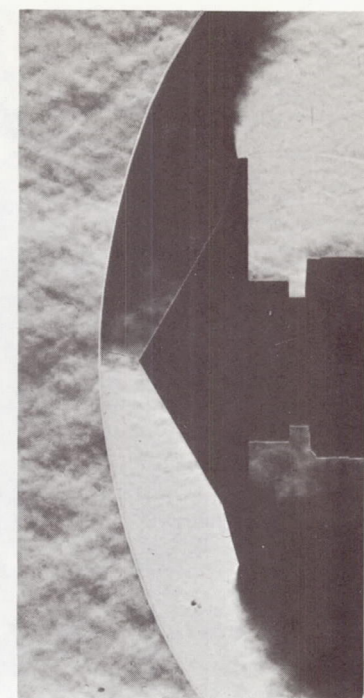
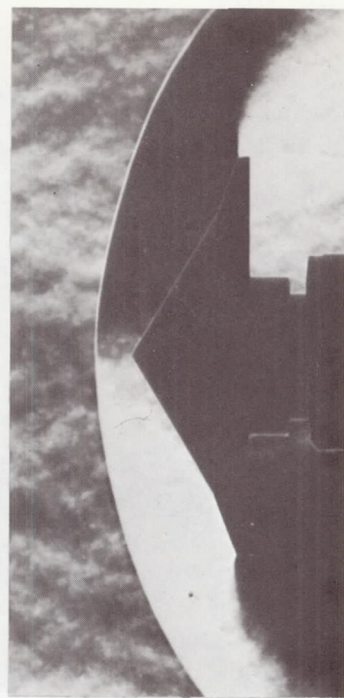
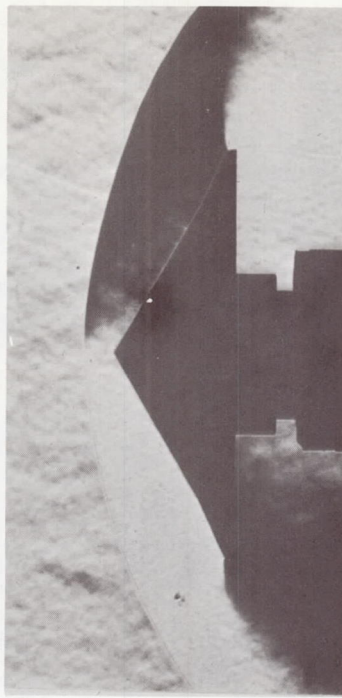


$150^\circ$  Cone

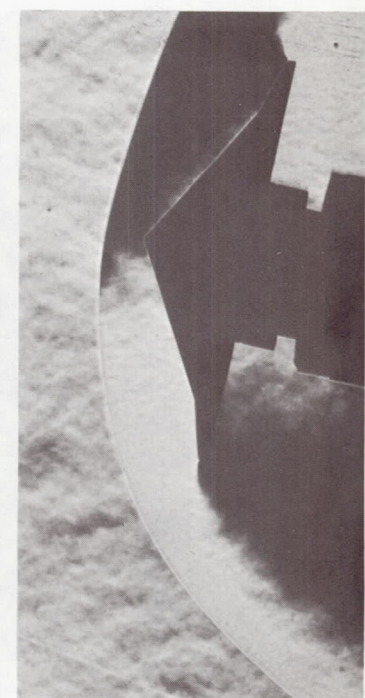
Figure 3.- Concluded.

L-68-10,084

$\alpha = 0^\circ$



$\alpha = 12^\circ$



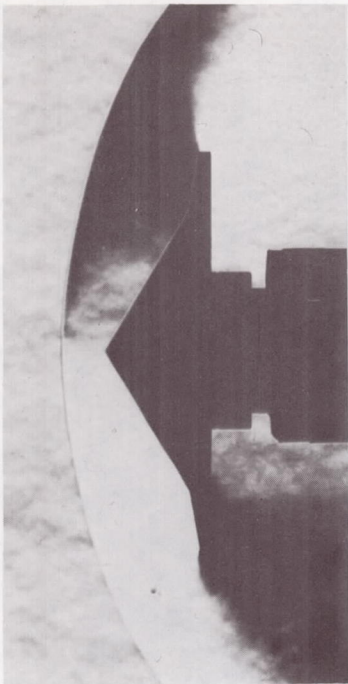
$\delta = 65^\circ$

$\delta = 70^\circ$

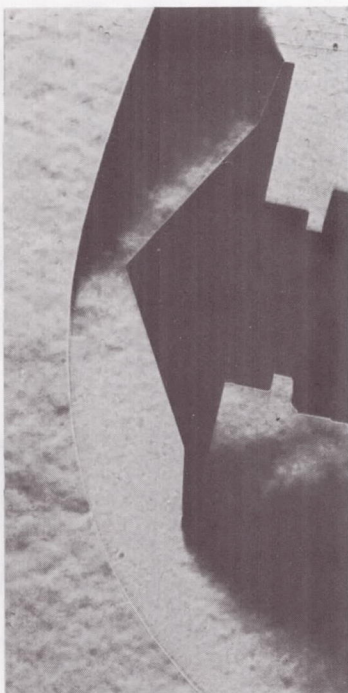
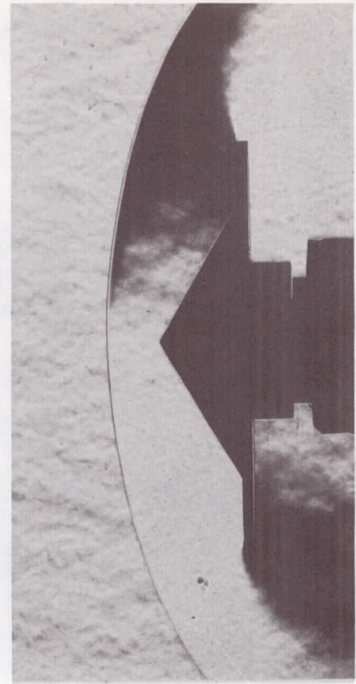
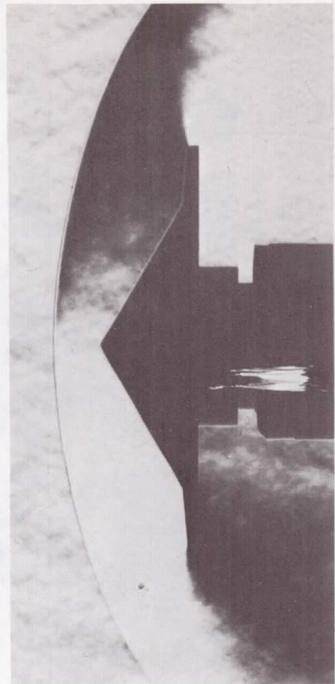
$\delta = 75^\circ$

Figure 4.- Schlieren photographs of flared cones at  $R \approx 1.1 \times 10^6$  and Mach 3.0.

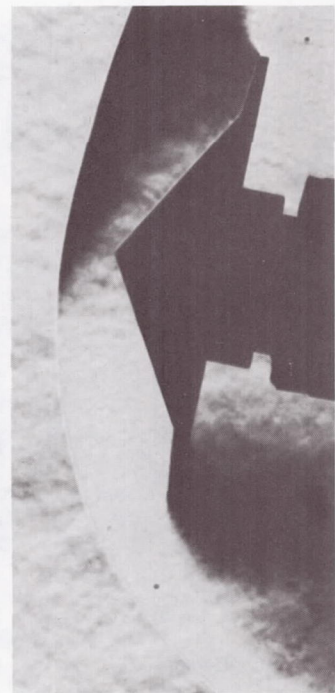
L-68-10,085



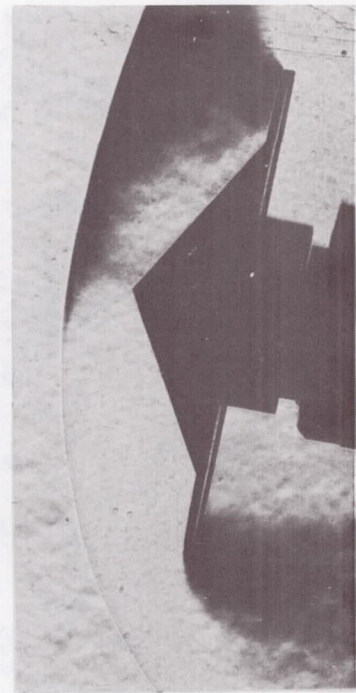
$\alpha = 0^\circ$



$\alpha = 12^\circ$



$\delta = 80^\circ$

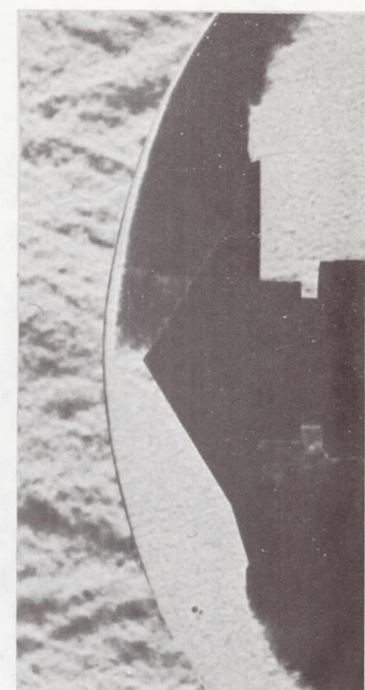
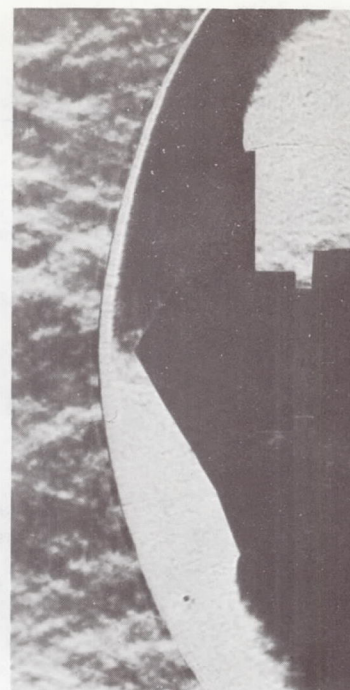
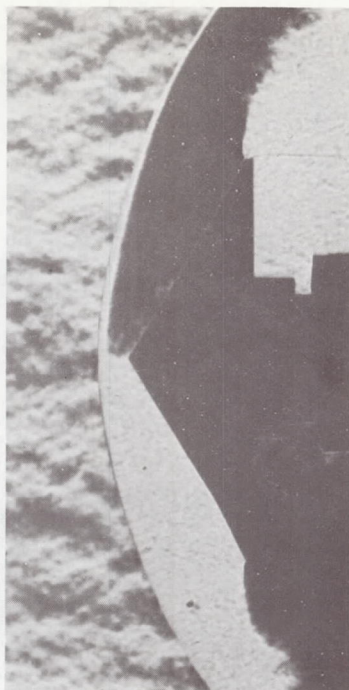


$\delta = 90^\circ$

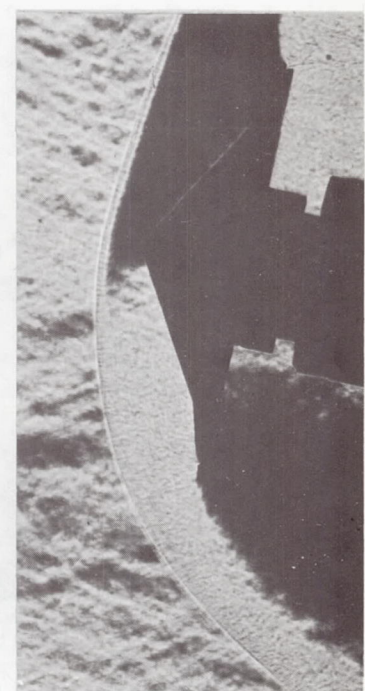
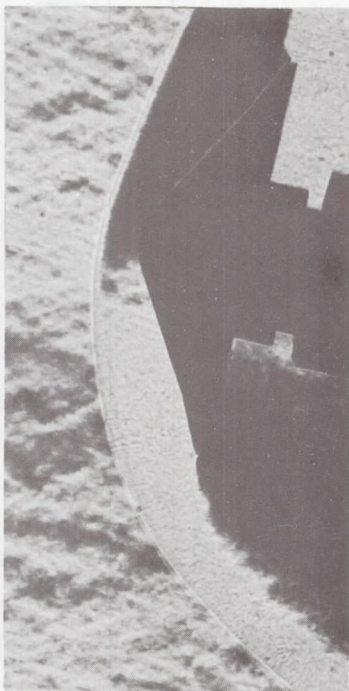
Figure 4.- Concluded.

L-68-10,086

$\alpha = 0^\circ$



$\alpha = 12^\circ$



$\delta = 65^\circ$

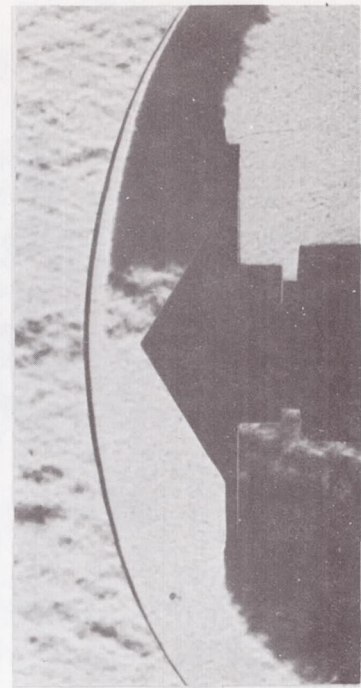
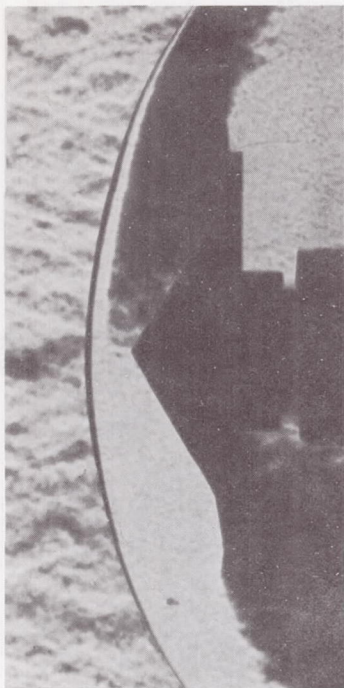
$\delta = 70^\circ$

$\delta = 75^\circ$

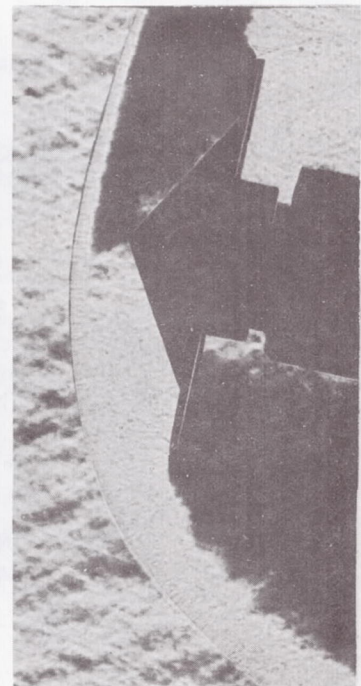
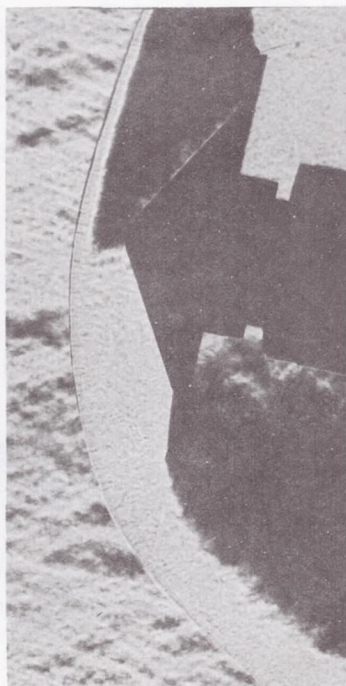
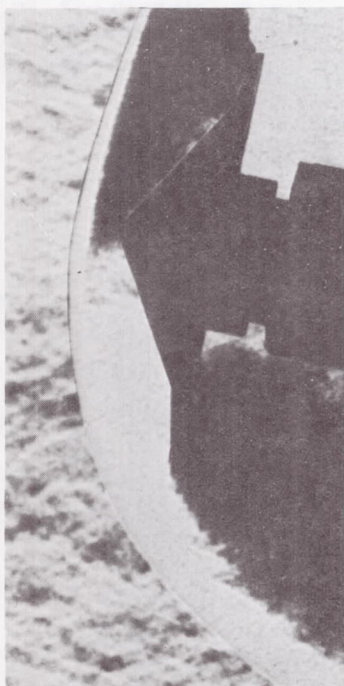
Figure 5.- Schlieren photographs of flared cones at  $R \approx 3.0 \times 10^6$  and Mach 3.0.

L-68-10,087

$\alpha = 0^\circ$



$\alpha = 12^\circ$



$\delta = 80^\circ$

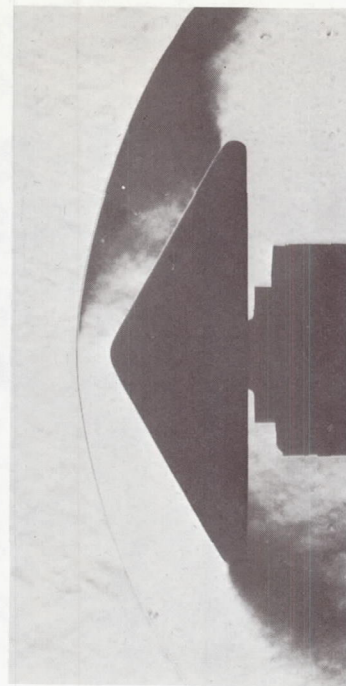
$\delta = 85^\circ$

$\delta = 90^\circ$

Figure 5.- Concluded.

L-68-10,088

$\alpha = 0^\circ$



$\alpha = 12^\circ$



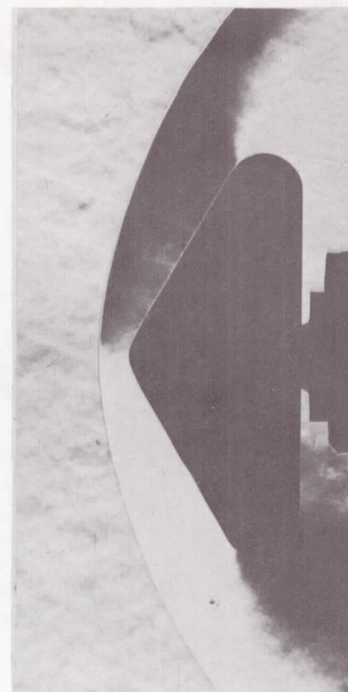
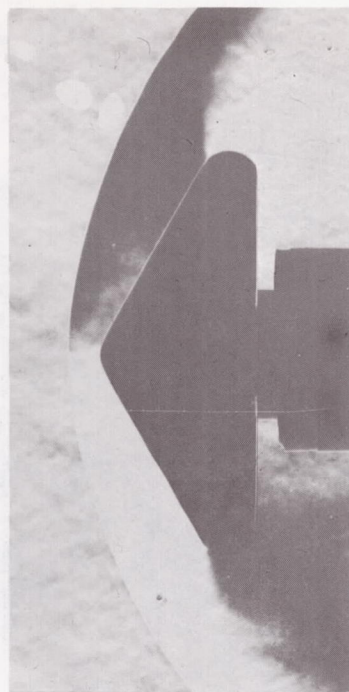
$$\frac{r_c}{r_b} = 0.05$$

$$\frac{r_c}{r_b} = 0.10$$

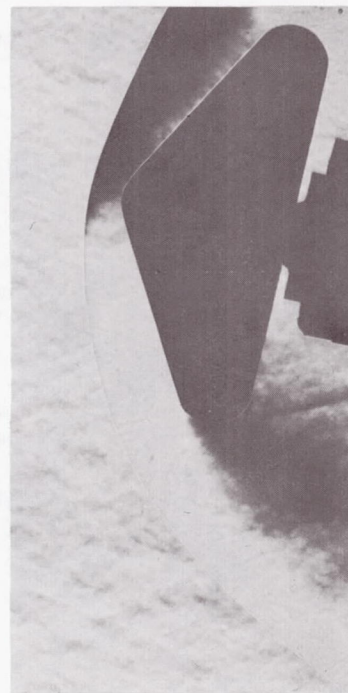
Figure 6.- Schlieren photographs of round-cornered cones at  $R \approx 1.1 \times 10^6$  and Mach 3.0.

L-68-10,089

$\alpha = 0^\circ$



$\alpha = 12^\circ$



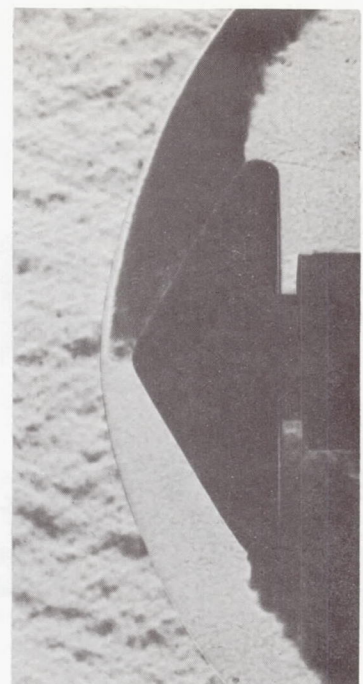
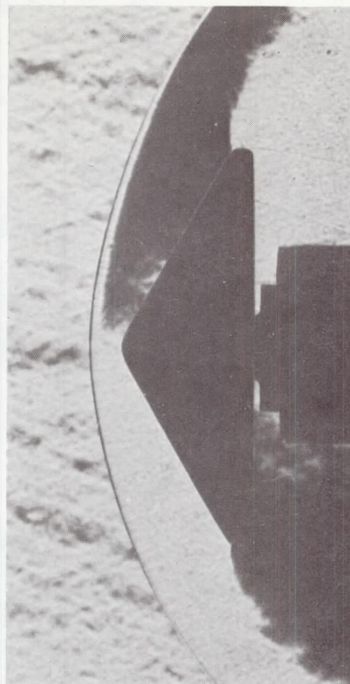
$$\frac{r_c}{r_b} = 0.15$$

$$\frac{r_c}{r_b} = 0.20$$

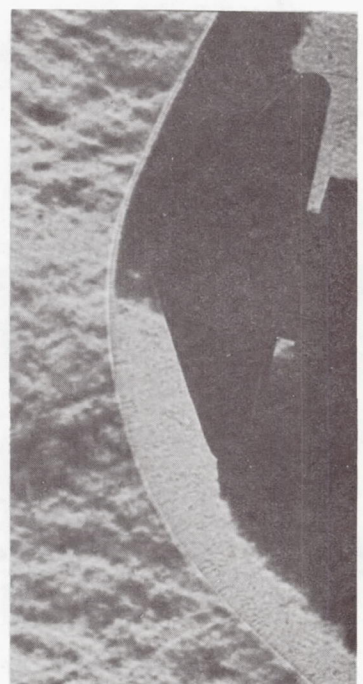
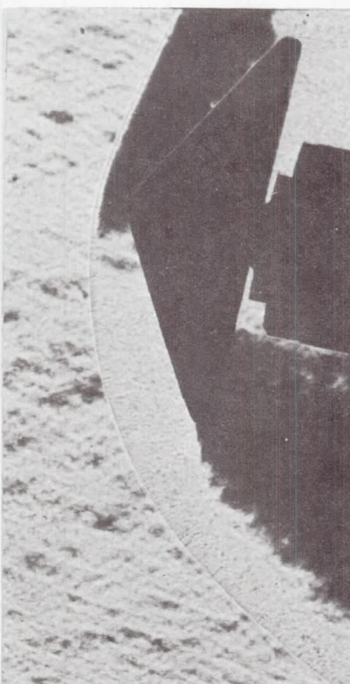
Figure 6.- Concluded.

L-68-10,090

$\alpha = 0^\circ$



$\alpha = 12^\circ$



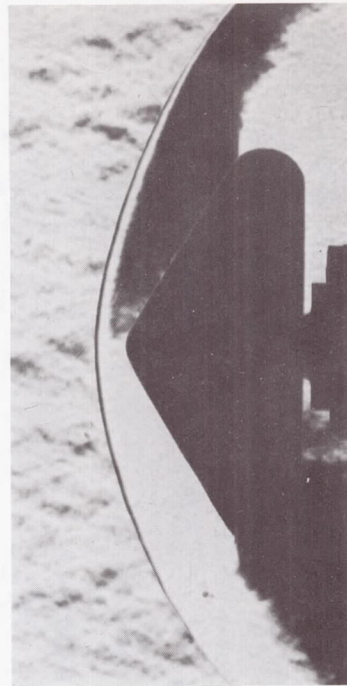
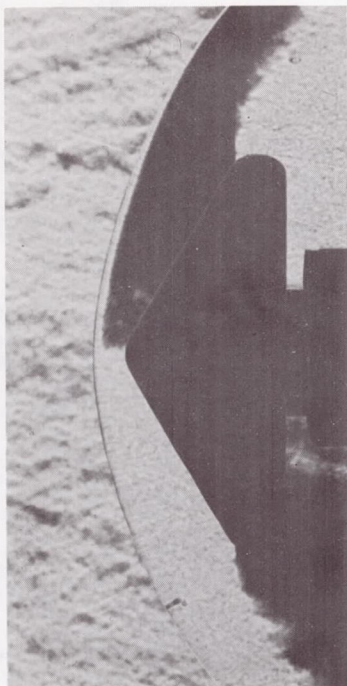
$$\frac{r_c}{r_b} = 0.05$$

$$\frac{r_c}{r_b} = 0.10$$

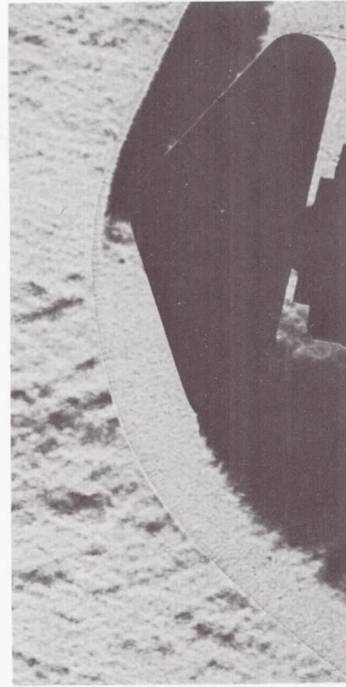
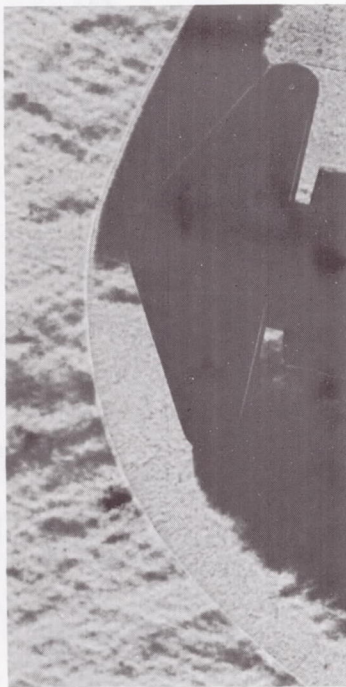
Figure 7.- Schlieren photographs of round-cornered cones at  $R \approx 3.0 \times 10^6$  and Mach 3.0.

L-68-10,091

$\alpha = 0^\circ$



$\alpha = 12^\circ$



$$\frac{r_c}{r_b} = 0.15$$

$$\frac{r_c}{r_b} = 0.20$$

Figure 7.- Concluded.

L-68-10,092

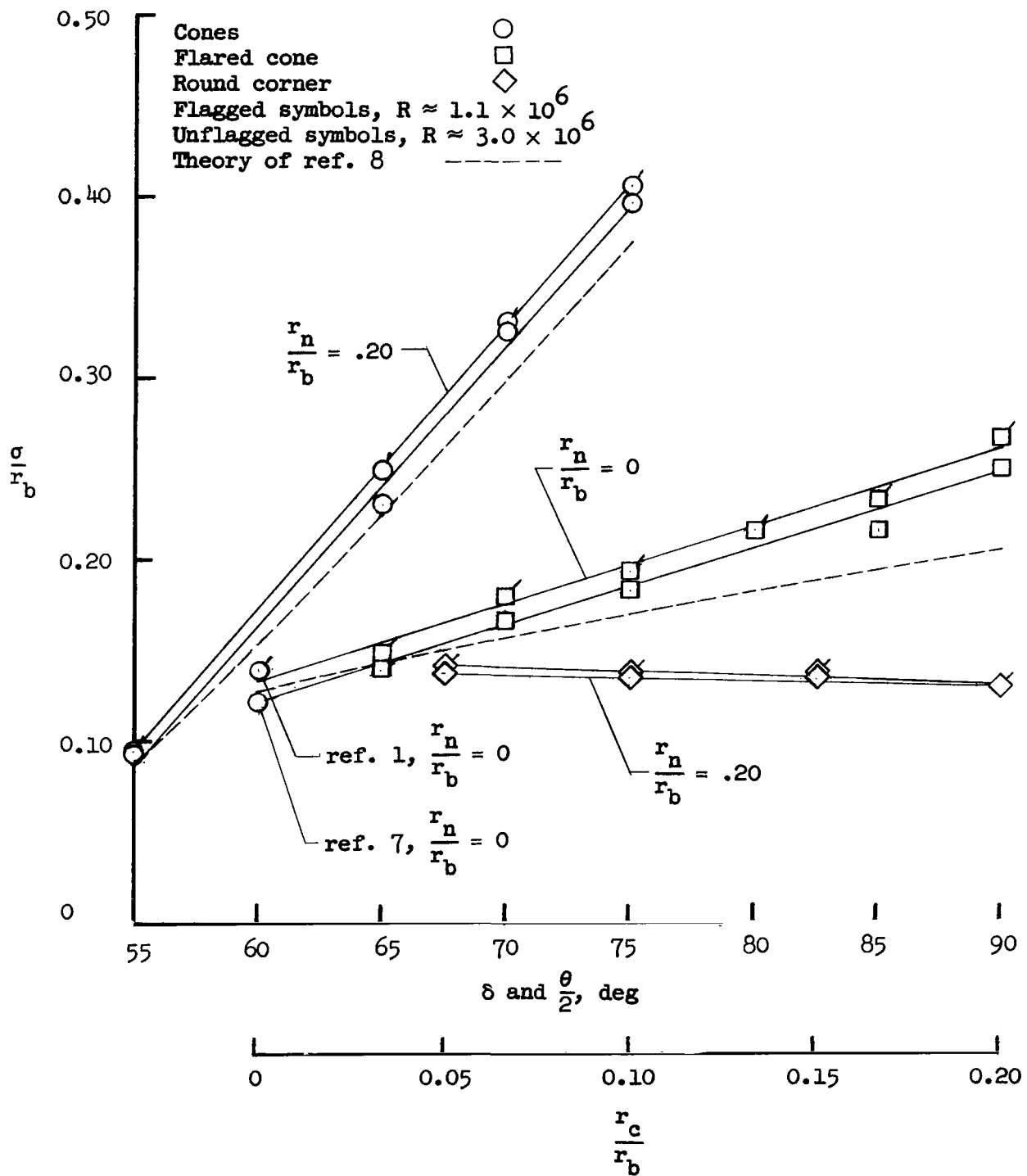


Figure 8.- Variation of shock-wave standoff distance with cone angle, flare angle, and corner radius at Mach 3.0.

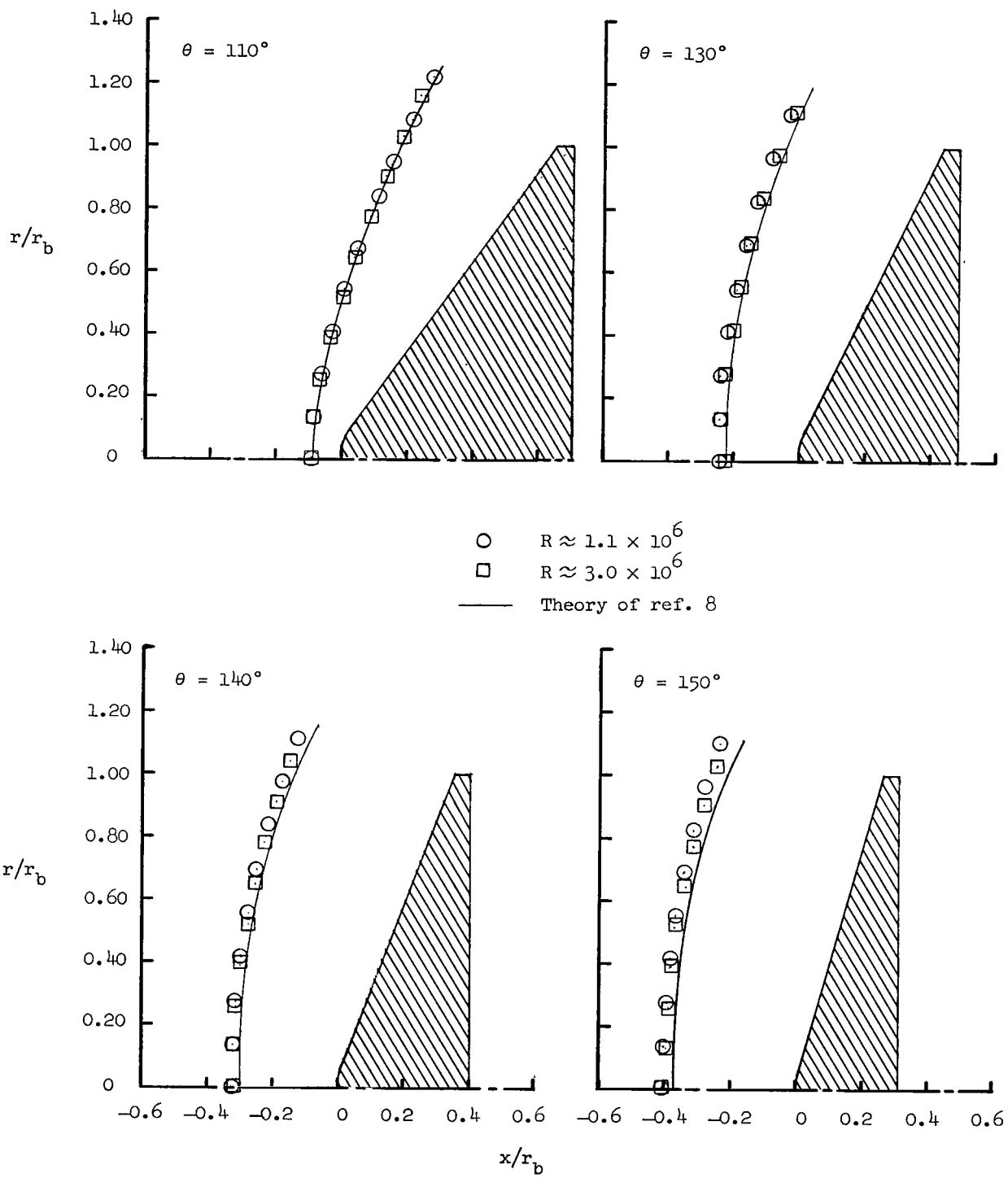


Figure 9.- Calculated and measured shock-wave shapes of large-angle cones at Mach 3.0.

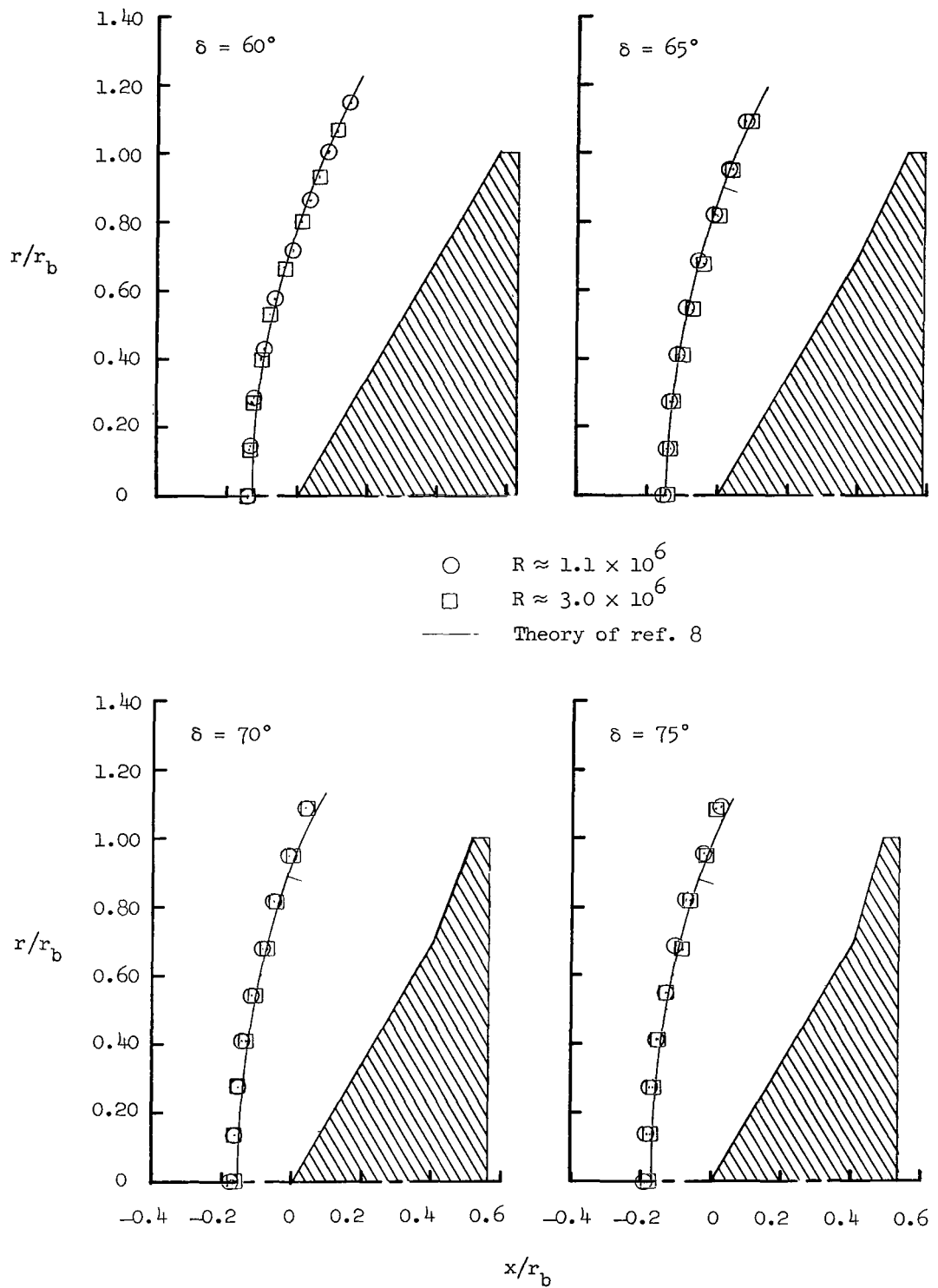


Figure 10.- Calculated and measured shock-wave shapes of flared cones at Mach 3.0.

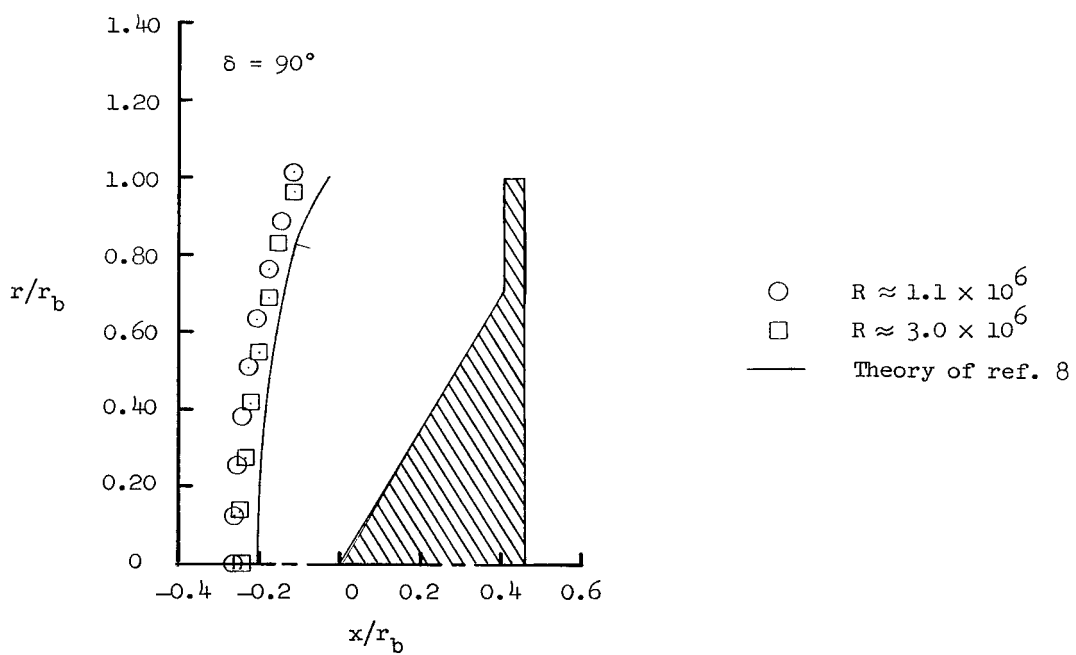
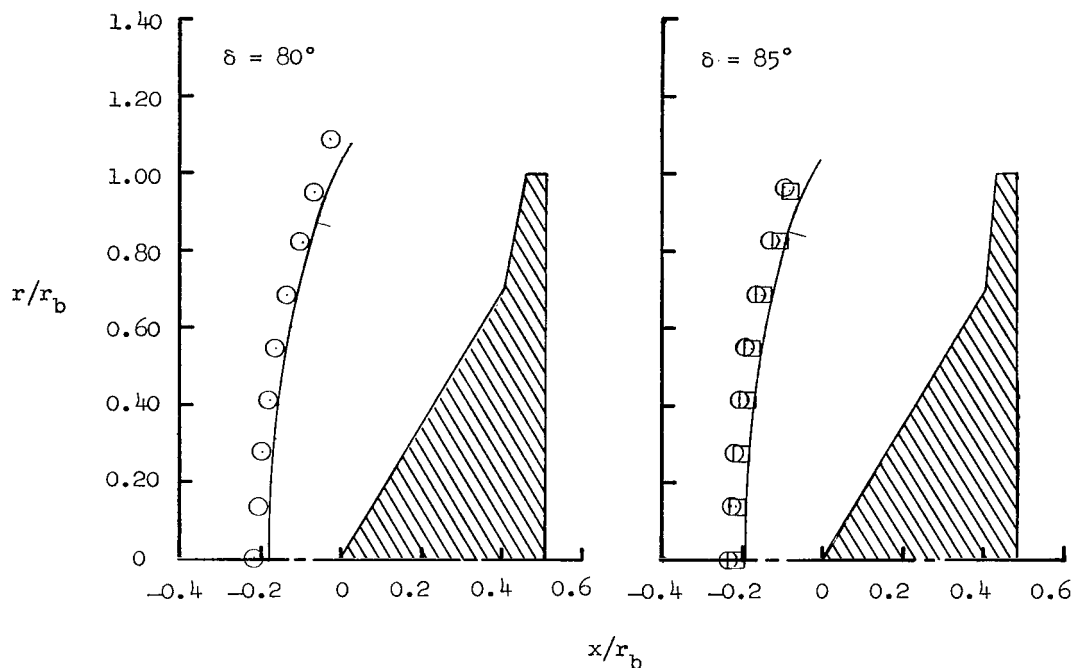
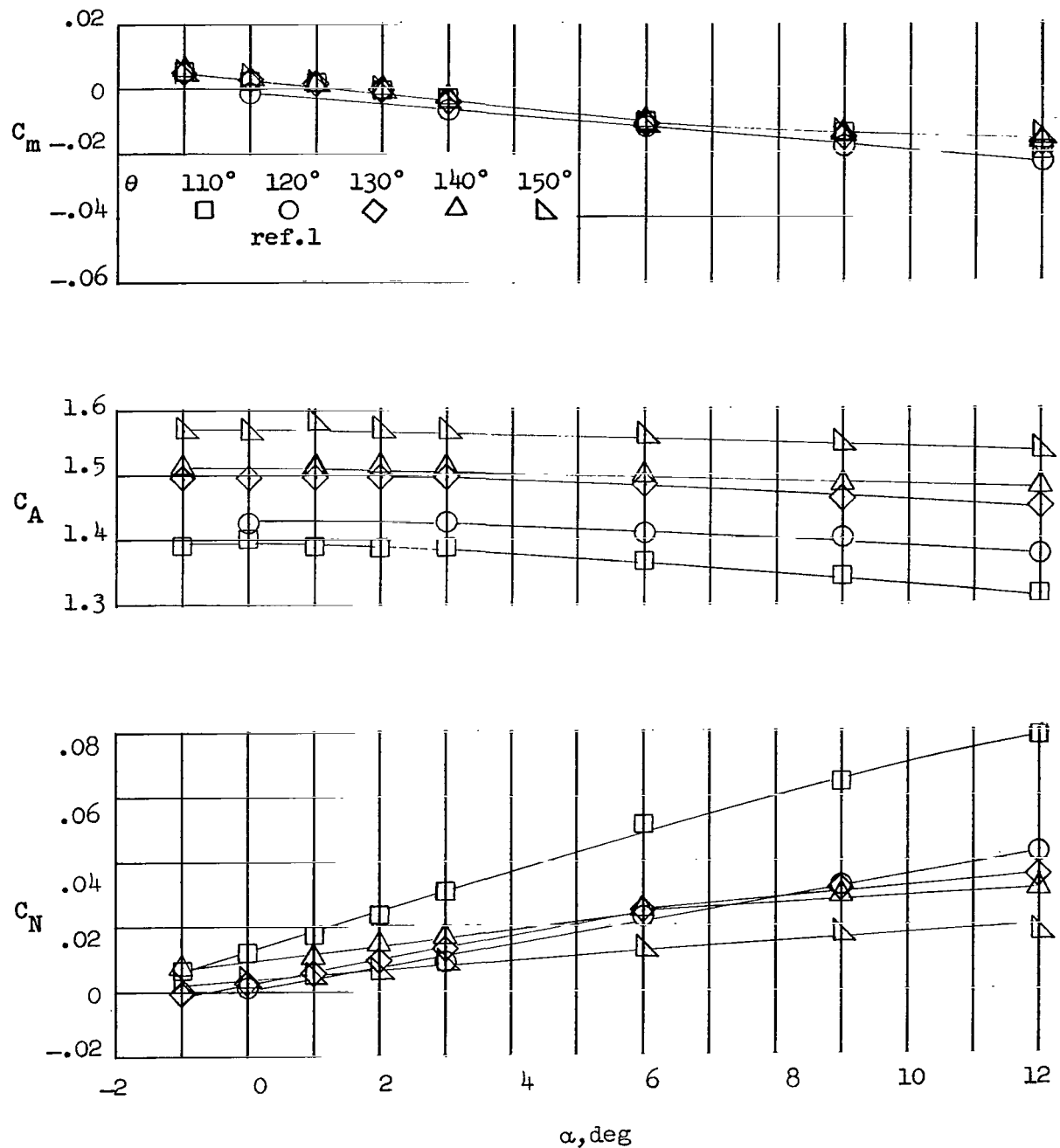
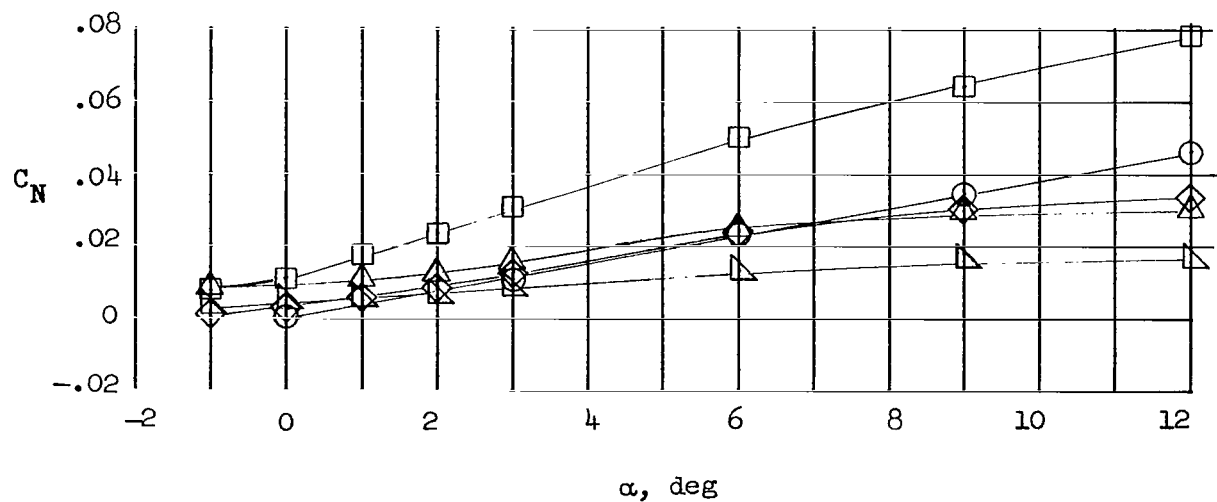
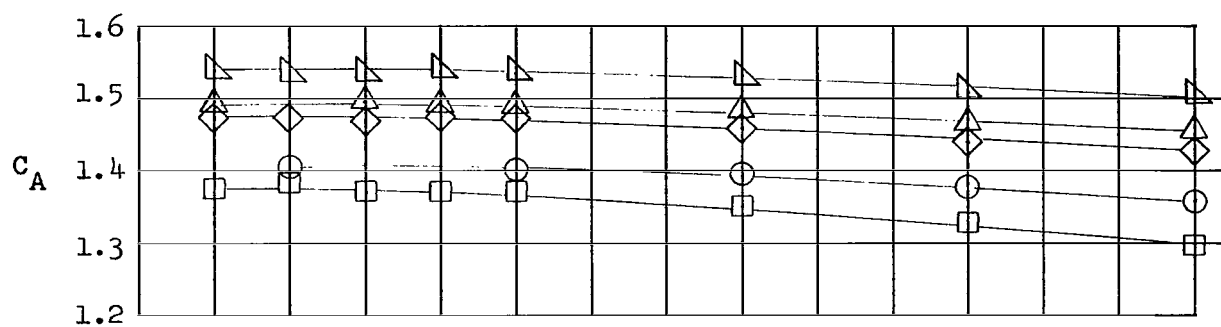
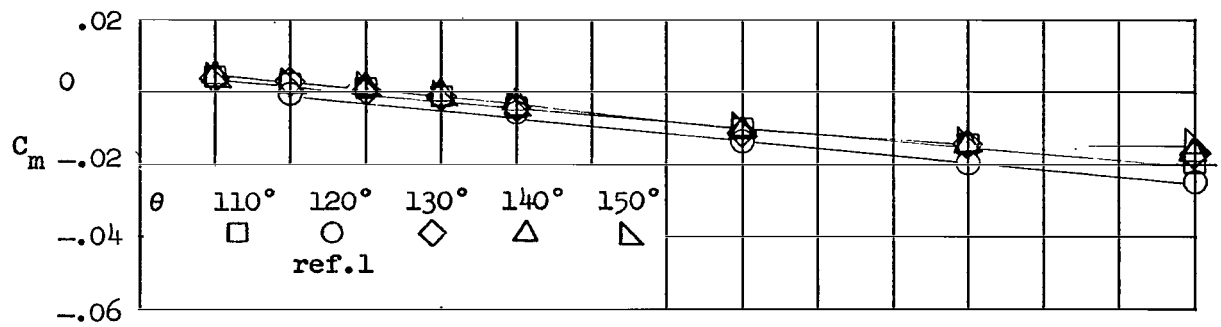


Figure 10.- Concluded.



(a)  $R \approx 1.1 \times 10^6$ .

Figure 11.- Longitudinal aerodynamic characteristics of large-angle cones at Mach 3.0.



(b)  $R \approx 3.0 \times 10^6$ .

Figure 11.- Concluded.

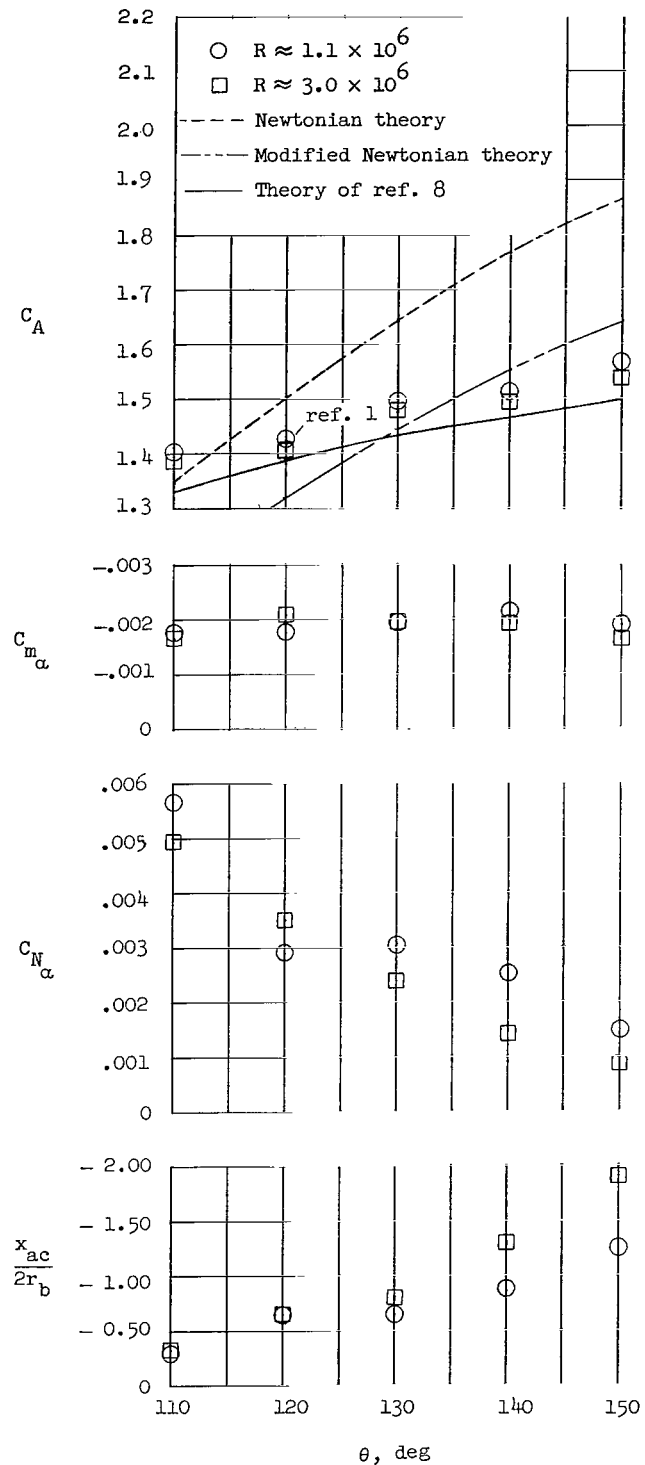
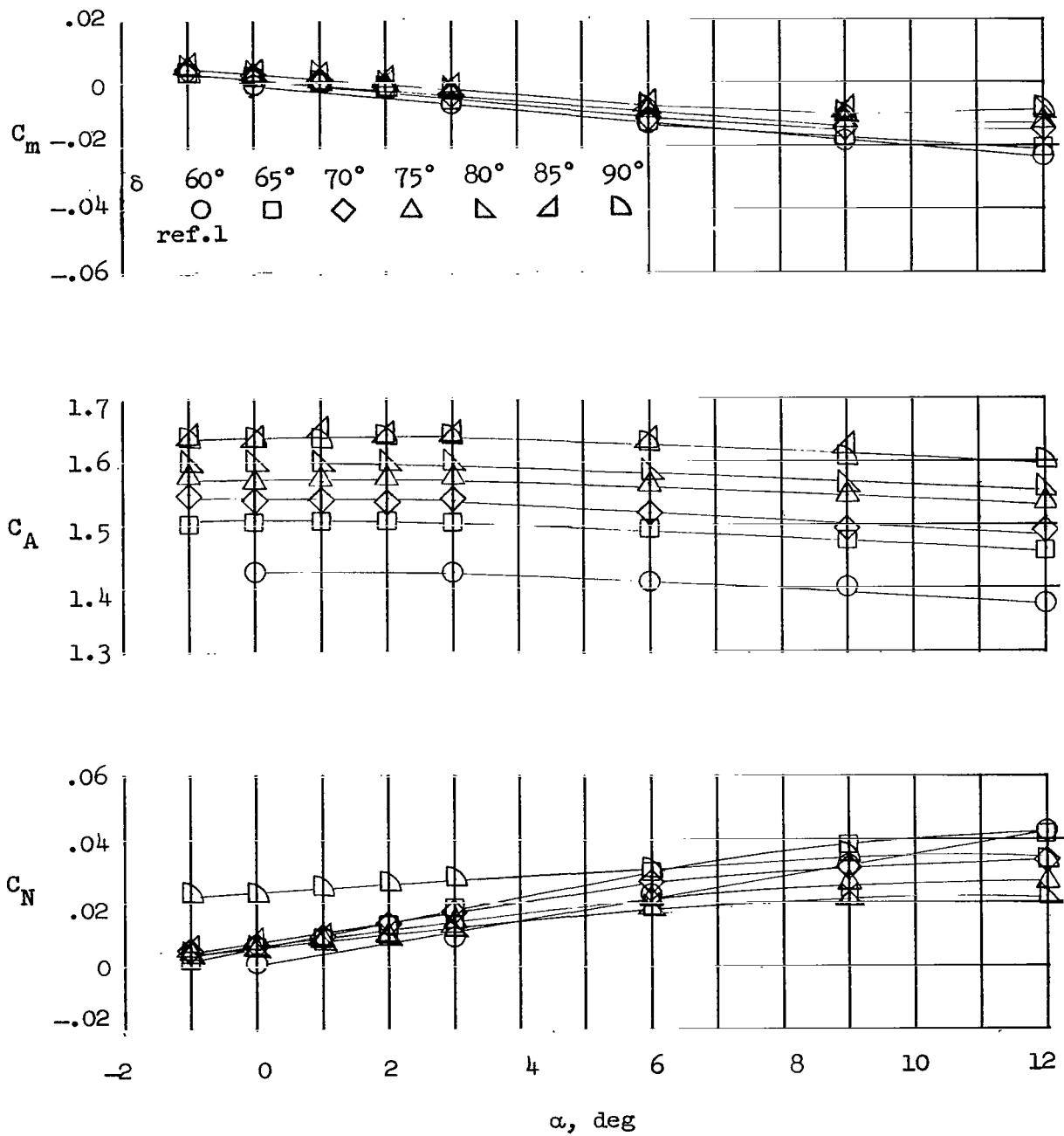
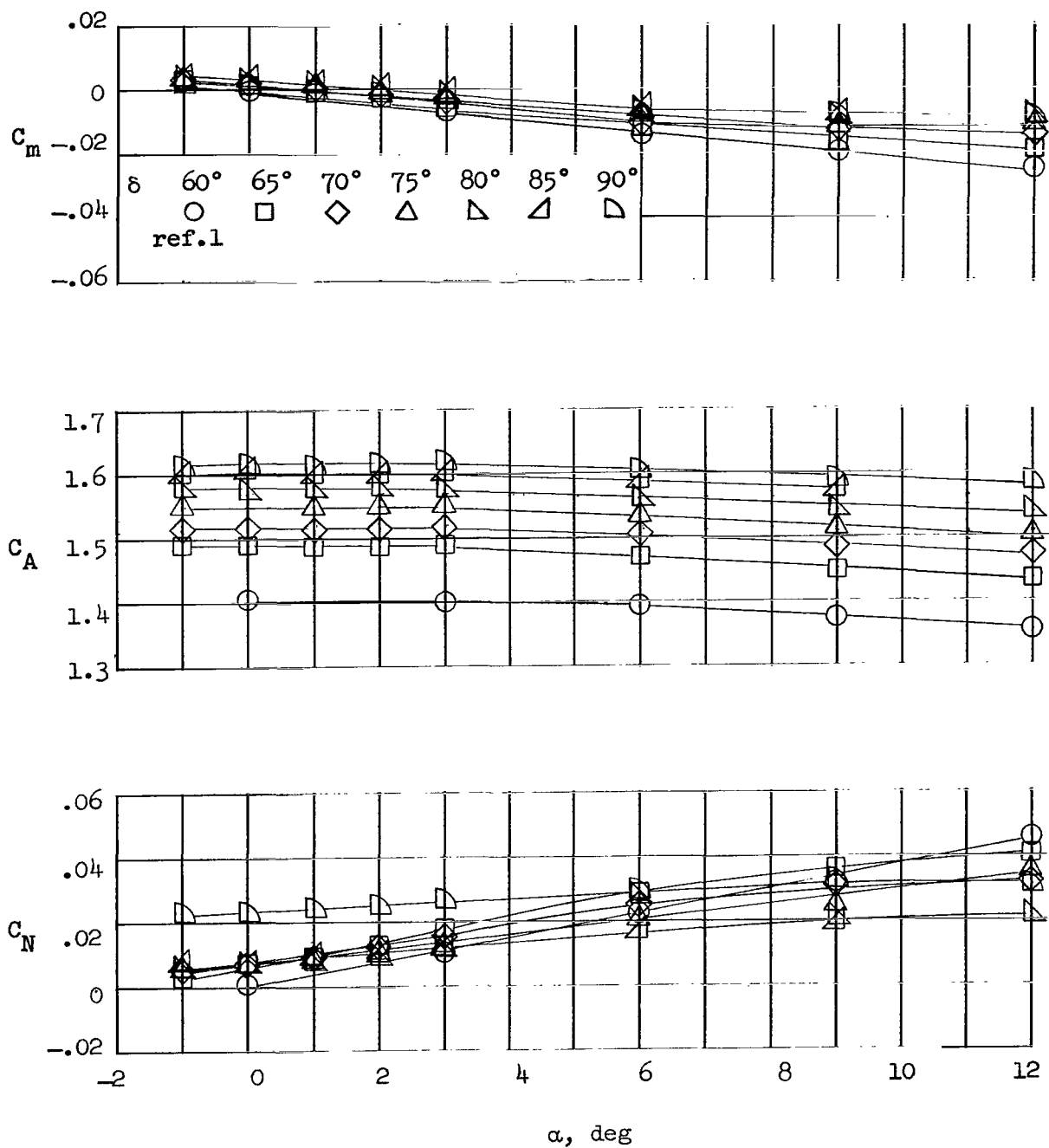


Figure 12.- Influence of cone angle on aerodynamic characteristics at  $\alpha = 0^\circ$  and Mach 3.0. (Test data at  $\theta = 120^\circ$  are from investigation of ref. 1.)



(a)  $R \approx 1.1 \times 10^6$ .

Figure 13.- Longitudinal aerodynamic characteristics of flared cones at Mach 3.0.  $\theta = 120^\circ$ .



(b)  $R \approx 3.0 \times 10^6$ .

Figure 13.- Concluded.

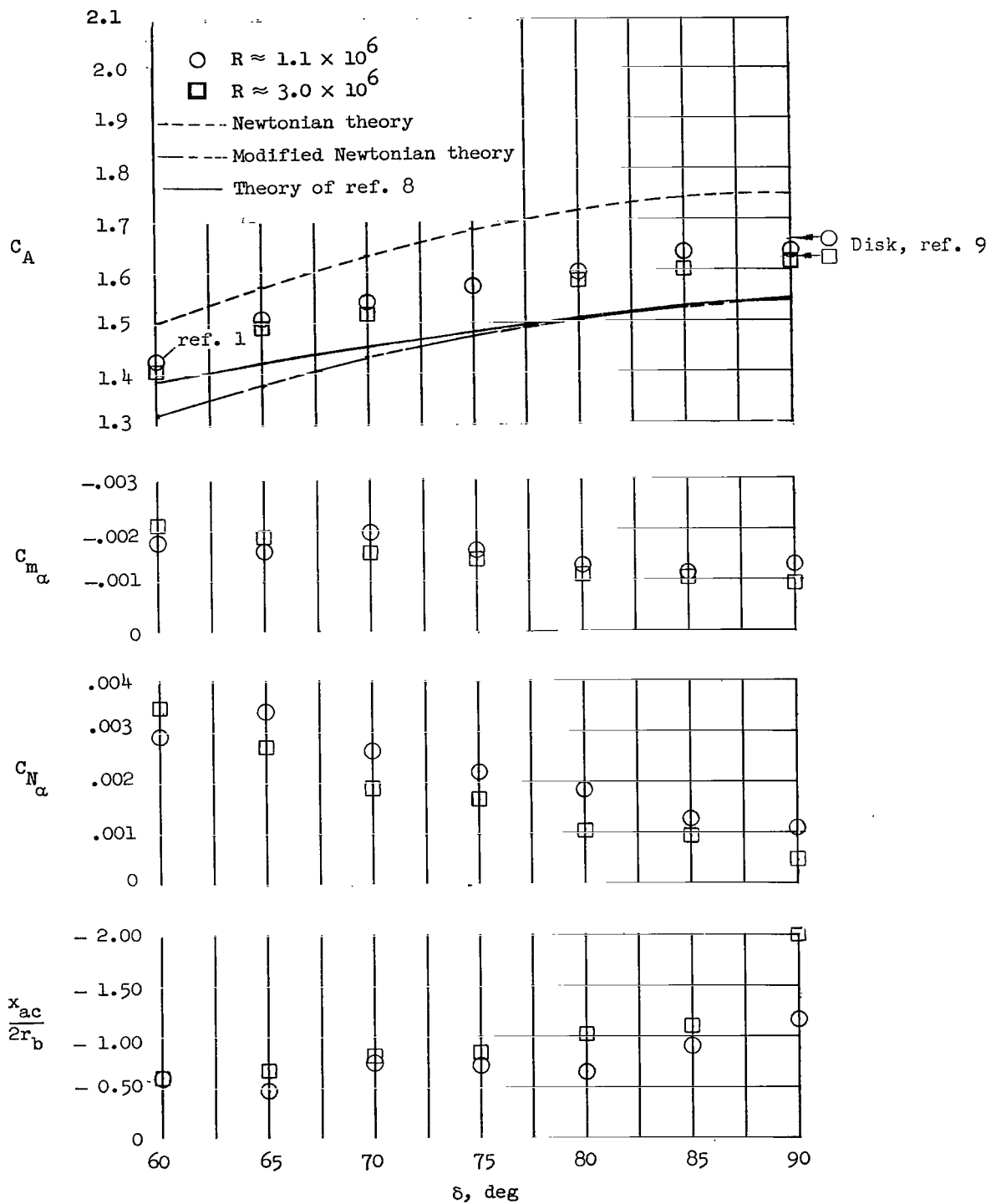
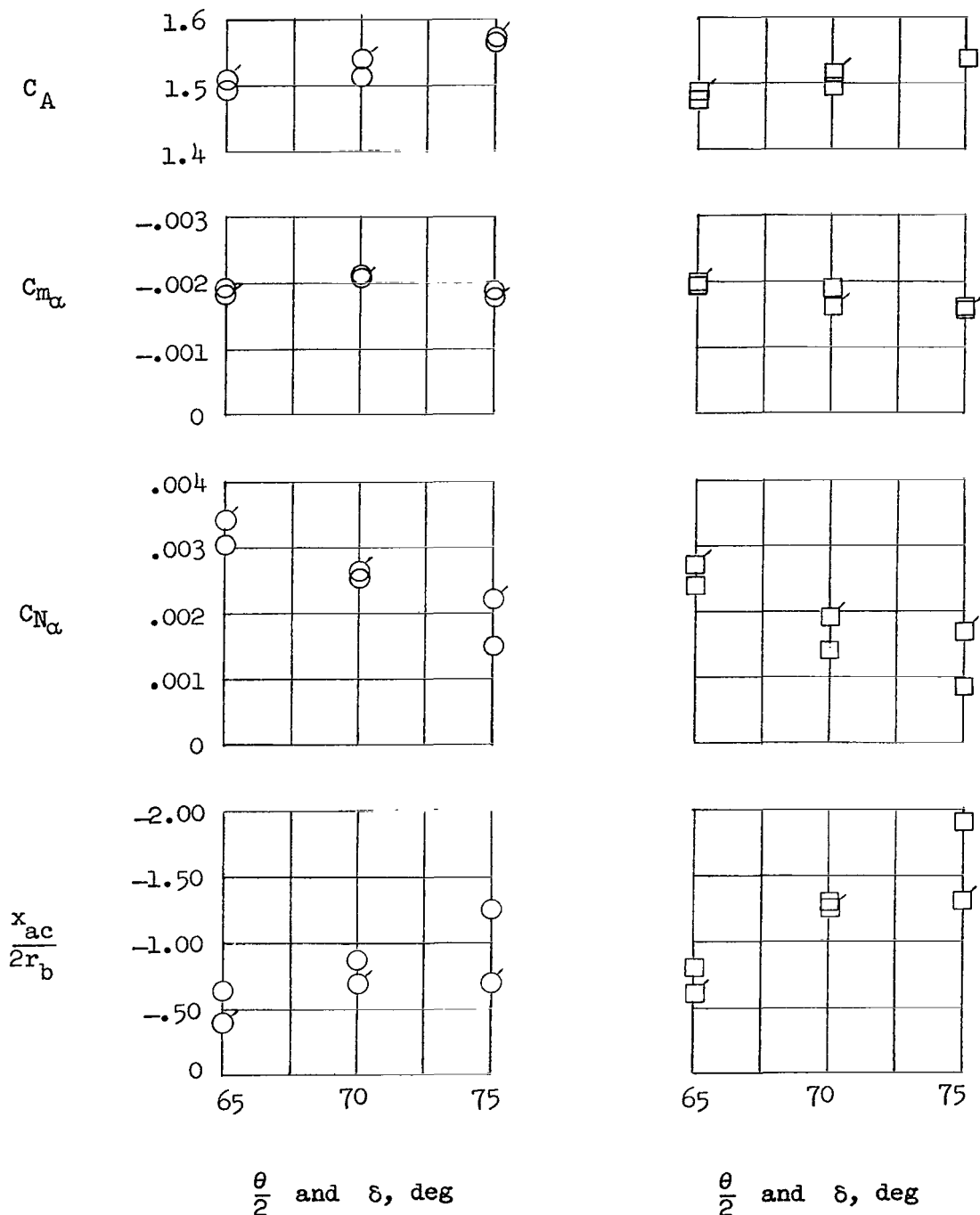


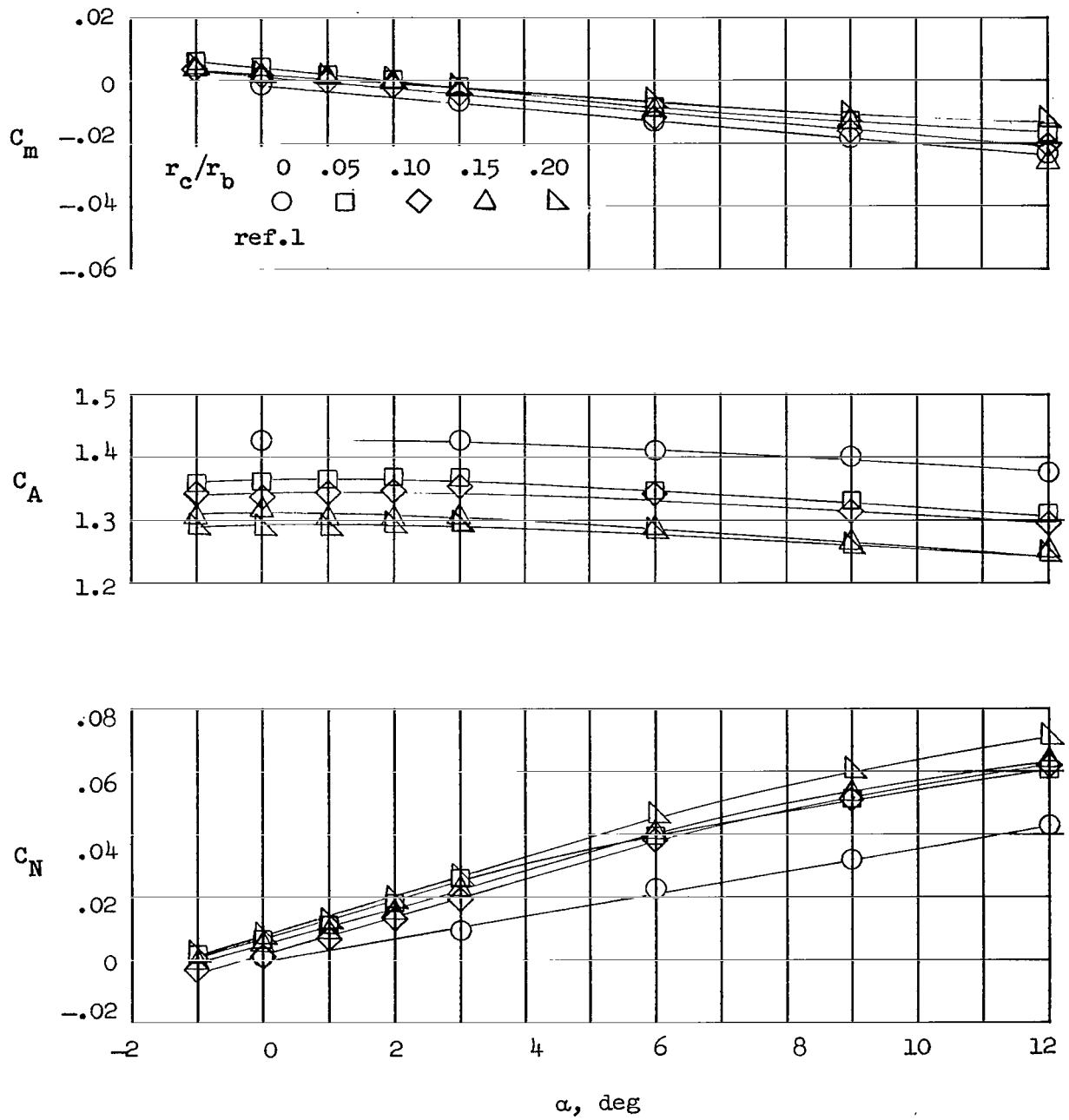
Figure 14.- Influence of base flare angle on aerodynamic characteristics of a  $120^\circ$  cone at  $\alpha = 0^\circ$  and Mach 3.0. (Test data at  $\delta = 60^\circ$  are from investigation of ref. 1.)



(a)  $R \approx 1.1 \times 10^6$ .

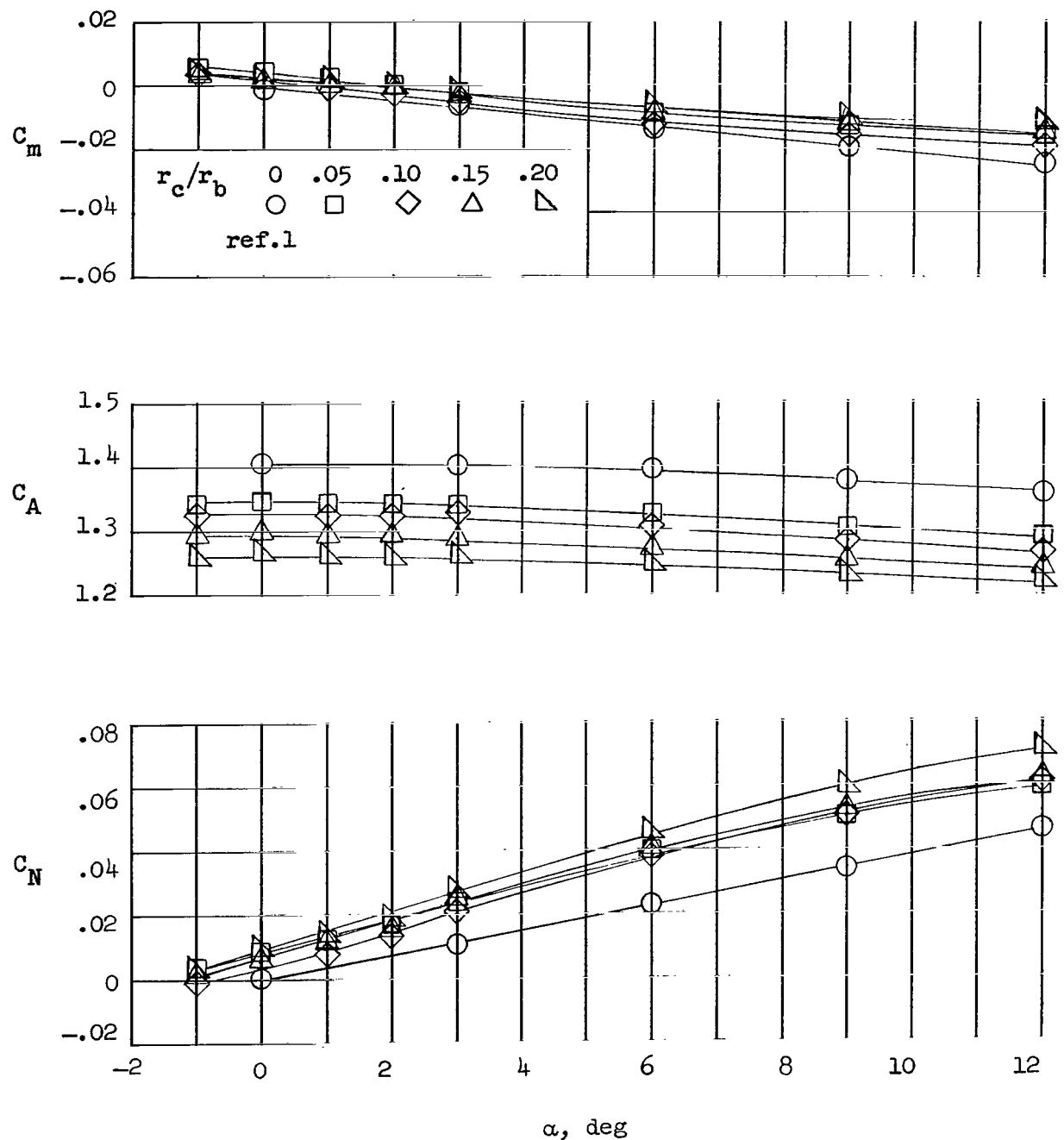
(b)  $R \approx 3.0 \times 10^6$ .

Figure 15.- Comparison of aerodynamic characteristics of cones and flared cones of equal flow turning angle. Flagged symbols denote flared-cone data.



(a)  $R \approx 1.1 \times 10^6$ .

Figure 16.- Longitudinal aerodynamic characteristics of round-cornered cones at Mach 3.0.  $\theta = 120^\circ$ .



(b)  $R \approx 3.0 \times 10^6$ .

Figure 16.- Concluded.

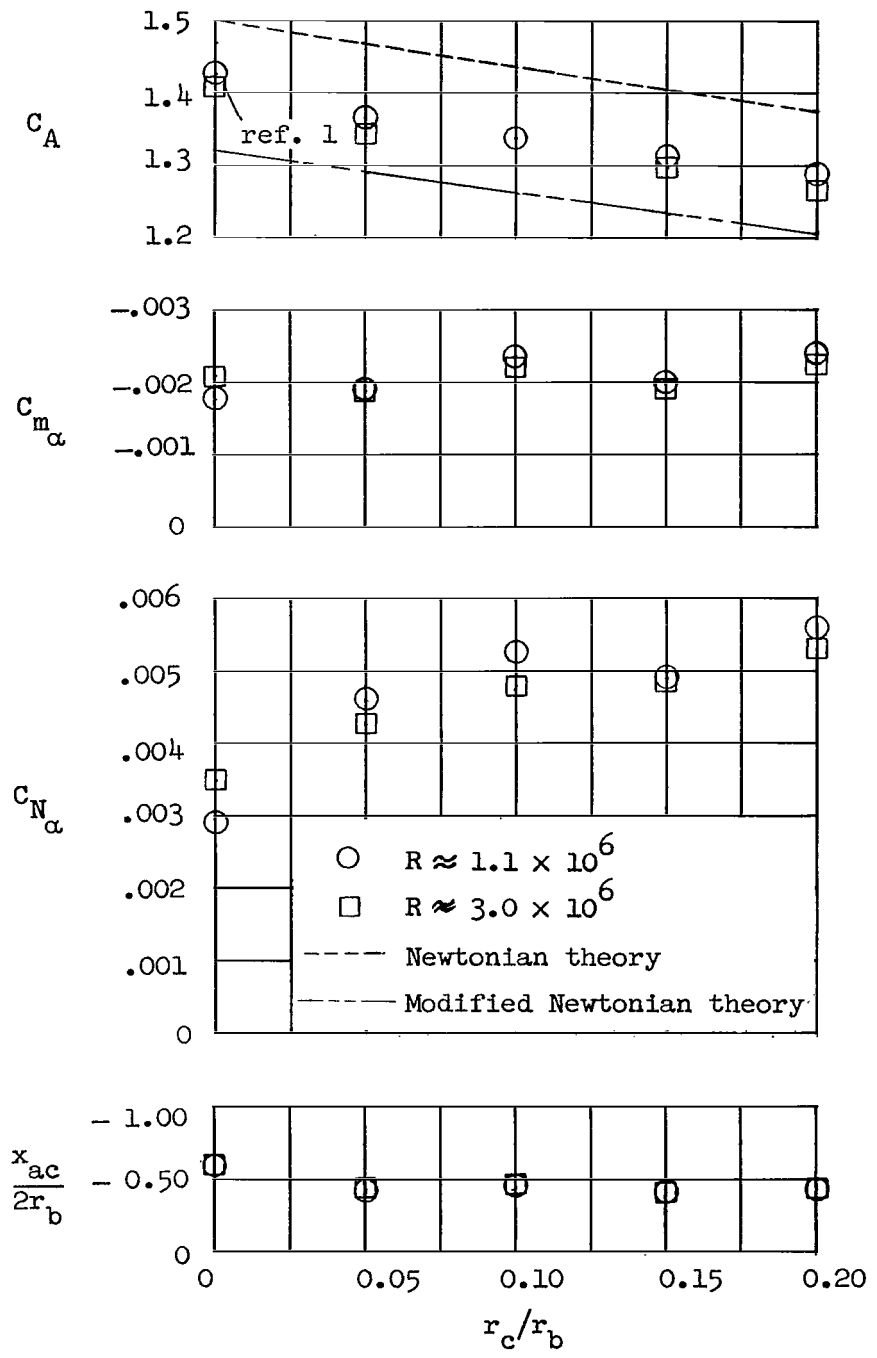


Figure 17.- Influence of base corner radius on aerodynamic characteristics of a  $120^\circ$  cone at  $\alpha = 0^\circ$  and Mach 3.0. (Test data at  $r_c/r_b = 0$  are from investigation of ref. 1.)